



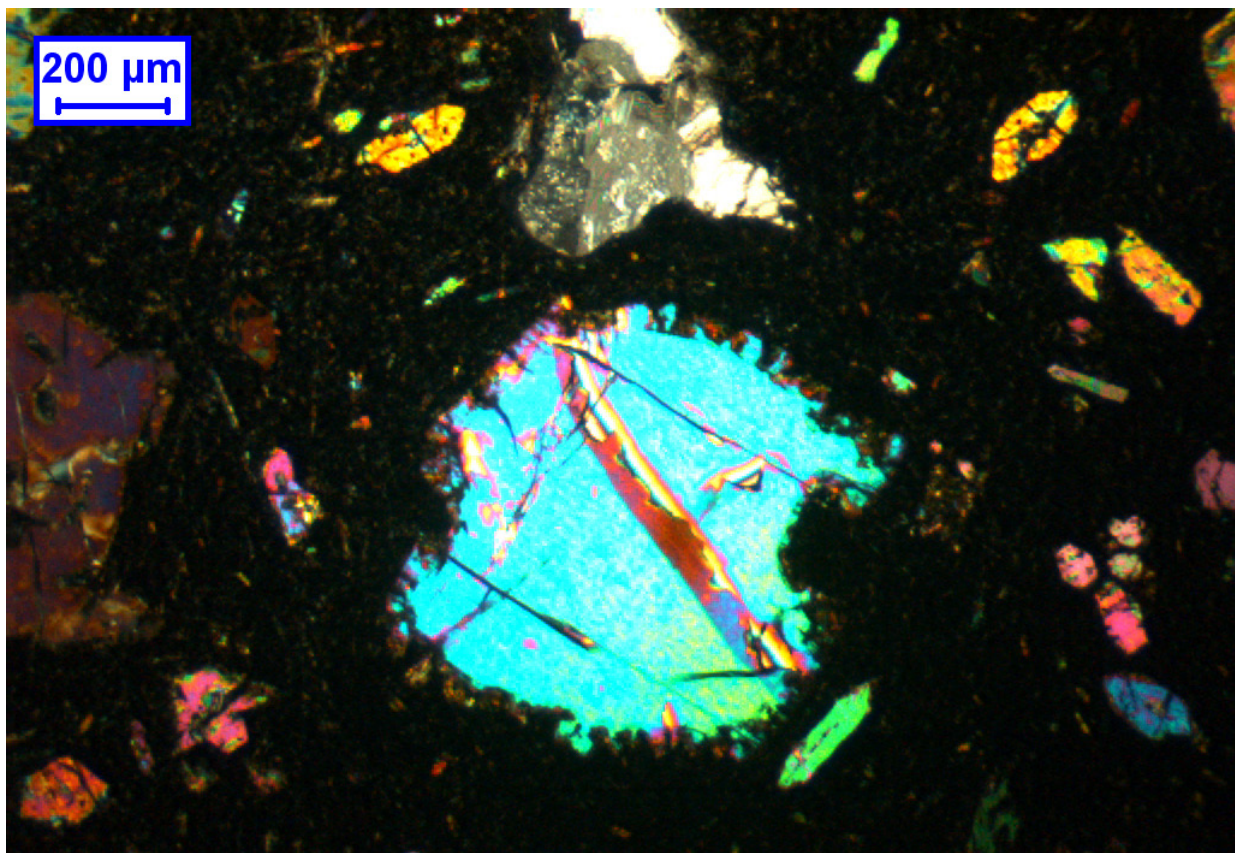
Stockholm
University

Master Thesis

Degree Project in
Geology 45 hp

Deciphering the origin of olivine crystals in alkaline magmas: The Calatrava Volcanic field, Spain

Hedvig Öste



Stockholm 2015

Department of Geological Sciences
Stockholm University
SE-106 91 Stockholm
Sweden

Deciphering the origin of olivine crystals in alkaline magmas: The Calatrava Volcanic field, Spain

Hedvig Öste

Abstract

The Calatrava volcanic province is one of four Cenozoic volcanic centers on the Iberian Peninsula, where volcanic activity occurred as the region was subjected to extension during collision between the African and the Eurasian plates. Mantle xenoliths have been reported from different lava types in the area. Previous studies indicate that some of these xenoliths represent metasomatised recycled mantle melts whereas others are not metasomatised. Olivine crystals in Calatrava magmas are present in distinct textural positions and display different stages of chemical breakdown. This implies that some of these crystals are xenocrysts and formed in different melts than those in which they are found. Using the magnesium number (Mg#) as a differentiation index and combining normalized electron microprobe compositional data of olivine crystals from lavas of the Calatrava district with the olivine distribution coefficient (K_D), the chemical composition of the parent melt has been determined. Olivine crystals display different levels of chemical breakdown and a range of Mg#, indicating that fractional crystallization occurred. There are also indications of some crystals having crystallized in a more primitive melt and were then transferred into a more evolved melt. In one sample, olivine is rimmed with a distinctly Mg-poor rim but the transition from core to rim occurs without obvious disequilibrium features and implies that these olivine crystals have crystallized from compositionally different, ultrabasic melts.

1. Introduction	4
2. Background	6
2.1 Geological Background	6
2.1.1 Regional Geology	6
2.1.2 Cenozoic Volcanic Provinces	7
2.1.3 The Calatrava Volcanic Province	7
2.2 Mantle end members	9
3. Field relations, sample collection and sample selection	9
3.1 Field relations	10
3.2 Site description	10
3.2.1 Sample selection	11
3.2.2 Secondary mineralization and xenoliths	12
4. Analytical methods	20
4.1 Petrography	20
4.1.1 Basalts	20
4.1.2 Melilitites	21
4.1.3 Nephelinites	22
4.1.4 Carbonate/carbonatite tuff with peridotite xenolith	23
4.2 Electron Microprobe	23
4.3 Calculations and modelling	26
4.3.1 Olivine crystallization	26
4.3.2 Distribution coefficients	26
4.3.3 Calculations	27
5. Mineral Chemistry	29
5.1 Electron microprobe analytical results	29
5.2 Magnesium numbers	30
5.3 Distribution coefficients	35
5.3.1 Whole rock compositions and distribution coefficients of phenocrysts	35
5.3.2 Calculating parental melt compositions	38

6. Discussion	39
6.1 Previous studies	39
6.1.1 Mantle metasomatism	39
6.1.2 Melilite and nepheline lavas	39
6.2 Magnesium numbers	40
6.3 Olivine distribution coefficient (K_D)	41
6.4 Crystal petrography and genesis	42
6.4.1 Basalts	42
6.4.2 Melilitites	43
6.4.3 Nephelinites	45
6.4.4. Geographical relations	46
6.4.5 Mineral assemblage	47
6.4.6 Presence of high-Fe Olivine crystals	47
6.5 Possible evolution of Calatrava field volcanism	48
7. Conclusions	49
7.1 Analysed samples	49
7.2 Non-analysed samples	49
7.3 Further studies	50
8. Acknowledgements	50
9. References	52
10. Appendices	55
10.1 Original EMP data	55
10.2 Mg# calculations	59
10.3 K_D calculations	63
10.3.1 K_D Calculations	62
10.3.2 Melt FeO/MgO ratio whole-rock composition	65
10.5 Thin section photographs with marked analytical points	66

1.Introduction

The Cenozoic era marks the onset of the continents moving towards the positions they inhabit today. As the African plate approached the Eurasian plate, the Alps were formed due to compression, Alpine orogeny, whereas other parts of Western Europe were subjected to extension and rifting (Cebriá and López-Ruiz 1994, 1996, Gibbons and Moreno 2002). The rifting may have generated melting of the underlying mantle, which rose through the old Precambrian and Paleozoic sediments that mostly comprise the Iberian Peninsula. Melting, mixing and perhaps partially assimilating the surrounding crustal rock, the magma interacted with groundwater and the volcanic activity was explosive, generating maar volcanoes, lapilli and volcanic bombs (Martín-Serrano et al. 2009). The eruptions also brought pieces of mantle peridotite to the surface, which are found at several outcrops within the Calatrava Volcanic field in Spain. Ultramafic mantle xenoliths, or xenocrysts of olivine and/or pyroxene in mafic rocks, are useful for obtaining information about the chemical composition of the mantle. Xenocrysts are crystals originated from another melt or rock than the one it currently inhabits. Phenocrysts are larger crystals inhabiting a fine-grained matrix, formed from the same melt as the groundmass (Winter, 2010). Petrographic, trace element and isotope studies can be used to determine the type of mantle beneath continents and can help us understand how the mantle has evolved (Gibson et al. 2008, Coltorti et al. 2010). The presence of ultrabasic phenocrysts in basic rocks implies several stages of magma crystallization and displacement of magma prior to eruption.

Mantle xenoliths in the Calatrava Volcanic field in central Spain have previously been reported by Cebriá and López-Ruiz (1996), Bailey et al. (2005), Bianchini et al. (2010), Humphreys et al. (2010) and Villaseca et al. (2010). Cebriá and López-Ruiz (1994 and 1996) focused on classifying the volcanic outcrops within the area in order to construct models of how and why volcanic activity occurred in Calatrava. Bailey et al. (2005) and Humphreys et al. (2010) examined possible evidence of carbonatite volcanism. Bianchini et al. (2010) proposed massive metasomatism of the mantle by Fe-Ti rich fluids to explain the high FeO-TiO content in peridotite xenoliths whereas Villaseca et al. (2010) suggested mixing between a depleted mantle and enriched, recycled mantle.

There are over 200 volcanic outcrops in the Calatrava district, however only a few have been studied in detail. Mantle xenoliths, aggregates of olivine phenocrysts, and olivine phenocrysts appearing to be in different stages of chemical breakdown, are present in many of the to date unstudied outcrops. Studying these olivine xenocrysts and phenocrysts may provide insight into the structure of magmatic plumbing systems underneath the surface. The magnesium # $[(\text{Mg}/\text{Mg}+\text{Fe}) * 100]$ is a differentiation index for olivine phenocrysts and provides information about the composition of the magma (basic or ultrabasic) in which the crystals were formed. The olivine distribution coefficient, which was experimentally established by Roeder and Emslie (1970) as 0.3, can be used to calculate the Mg/Fe ratio of the parent melt (Roeder and Emslie, 1970, MacLennan, et al. 2003).

In the field, peridotite xenoliths were only observed in one outcrop. In several outcrops, aggregates of olivine crystals appear as megacrysts together with smaller crystals in a very fine-grained to aphanitic matrix. These olivine crystals were studied in thin section under the microscope and analysed with an electron microprobe (EMP). The microscopy studies focused on identifying one or several populations of olivine crystals in the samples optically and texturally, via condition of the crystals, i.e.- euhedral to skeletal crystal appearance, reaction rims, etc. From this preliminary assessment suitable samples were selected for EMP analysis to determine the Mg/Fe ratios in the most pristine olivine crystals. The aim of this study is to determine the origin of olivine crystals found in the Calatrava basic lavas.

2. Background

2.1 Geological Background

2.1.1 Regional Geology

The Iberian Peninsula is located in SW Europe and consists of the countries Spain, Portugal, Andorra and Gibraltar (Fig. 1). Spain is mainly comprised of the Precambrian through Paleozoic Iberian massif in the west together with Meso- and Cenozoic sedimentary basins in the east (Gibbons and Moreno 2002). Throughout the Iberian massif, outcrops of Precambrian sedimentary and metasedimentary rocks are found. In the northernmost part, shales, schists and sandstones with intrusions of Neoproterozoic high-K calc-alkaline diorites and metapelites, metasandstones and metavolcanics are preserved in antiforms. In the central parts of the massif, Central Iberian Zone, CIZ, Precambrian rocks comprise Neoproterozoic arkoses with overlying shale, sandstone, limestone and gneiss. Little deformed sandstone and conglomerates are also found (Valladares et al. 2002). The dominant sedimentary units of the Paleozoic sediments include Cambrian and Carboniferous siliclastic sediments and Ordovician fossil-bearing siliclastic sediments. During the Silurian period, the siliclastic sediments grade into graphite-bearing black shales. These sediments were deposited on the continental margin of Gondwana (Gibson and Moreno, 2002) and as Gondwana and Laurentia-Baltica began to converge during the Devonian period, Carboniferous sediments were deposited in supratidal to subtidal waters, prior to Variscan, also known as Hercynian, orogeny. Thick sedimentary deposits and well-preserved fossils from this period can be found in several outcrops, e.g. in the western Pyrenees (Colmenero et al. 2002). As Gondwana, Laurentia-Baltica and several microcontinents lying in-between, collided during Variscan orogeny towards the end of the Carboniferous, the sedimentary basin began to deform and metamorphose and the sediments were eventually uplifted. Syn- and post-tectonic magmatism generated granitoids that now comprise part of the massif. The Pyrenees in the north, at the border with France, also partially comprise Paleozoic granitoids and granitoids generated during the Variscan orogen (Ábalos et al. 2002). In the Late Carboniferous the tectonic setting changed from compressional to extensional, causing rifting and the opening of the Tethys Ocean at the end of the Paleozoic (Latest Carboniferous-Early Permian) and early Mesozoic (Triassic). The thinning of the crust resulted in dioritic intrusions in the Iberian massif and the Pyrenees. The break up of Laurentia-Greenland and Fenno-Sarmatia from Gondwana by the

opening of the Tethys Ocean placed the Iberian massif near the continental shelf and new sedimentary basins developed (López-Gómez et al. 2002). Sedimentation continued through the Mesozoic and Cenozoic eras. Continued extension and the opening of the Bay of Biscay during Cretaceous generated the independent microcontinent of Iberia. From the mid-Cretaceous until the Miocene, the continents once again began to converge. The Iberian microcontinent was driven towards the Eurasian plate. The Bay of Biscay was subducted underneath Iberia and eventually Iberia became partially subducted underneath Eurasia. The Mesozoic and Cenozoic sedimentary basins were uplifted and partially deformed during the onset of Alpine Orogeny (Gibbons and Moreno, 2002).

2.1.2 Cenozoic Volcanic Provinces

The presence of Cenozoic volcanism is explained as the result of crustal thinning caused by the welding of the Betic Cordillera onto the Iberian plate. This was part of the Alpine Orogen, which resulted from the collision of the African and Eurasian plates (Cebriá and López-Ruiz, 1994, 1996, Gibbons and Moreno 2002). The welding resulted in extension and initiated rifting of the crust within the entire Iberian foreland. The rifting formed a complex pattern of fractures oriented E-W to ENE-WSW, NW-SE and NE-SW, and graben structures oriented NW-SE. Three separate neotectonic events are recognized: 1) Initial extension during Miocene time resulted in the development of a sedimentary basin and the extrusion of leucitites; 2) continued rifting during the Pliocene resulted in the opening of the La Mancha basin that also allowed the extrusion of Pliocene basalts; 3) the third event was weak Pliocene regional compression. (Cebriá and López-Ruiz, 1994, 1996, Gibbons and Moreno 2002, Cebriá et al. 2011).

There are four known Cenozoic volcanic provinces in the Iberian Peninsula: the North-East (NEVP), South-East (SEVP), Gulf of Valencia (GVVP) and the Calatrava Volcanic Province (CVP). Of these, the GVVP is the least studied as it is located within the Mediterranean Sea. However, the few data indicate that the GVVP comprises calc-alkaline and alkaline basalts. The NEVP is mainly comprised of alkaline basalts with occasional leucitites, whereas the SEVP comprises alkaline, calc-alkaline, high-K calc alkaline, shoshonitic and ultrapotassic basalts (López-Ruiz et al. 2002). The CVP is discussed below.

2.1.3 The Calatrava Volcanic Province

The CVP is located within the Iberian massif (Fig. 1) and mainly consists of uplifted

Paleozoic sediments overlain by Cenozoic sediments (Colmenero et al. 2002). It was formed about 5.3-2.5 Ma years ago (Pliocene). Magmatic extrusion is believed to have occurred at Calatrava due to weakening of the crust by mantle diapirism. The volcanic activity was characterized by Strombolian and hydromagmatic eruptions, resulting in the formation of cinder cones, lava flows and maar craters. There are about 200 volcanic outcrops that are chemically classified into four rock types: olivine melilitite (OLM) which is basalt that contains the mineral melilite, olivine nephelinite (OLN) which is basalt that contains the mineral nepheline, alkaline olivine basalts (AOB) where melilite and nepheline are absent, and olivine leucitites (LEU) which contains leucite (López-Ruiz et al. 1994, 1996).

Trace element modelling of leucitites show that they are the result of batch melting and involved the subcontinental lithosphere (Cebriá and López-Ruiz 1994, 1996). The basalts, on the other hand, are the result of various degrees of fractional melting (described in detail by Cebriá and López-Ruiz 1994, 1996). $^{87}\text{Sr}/^{86}\text{Sr}$ and $^{143}\text{Nd}/^{144}\text{Nd}$ isotopic ratios show that the leucitites originated from a different depleted mantle source than the basalts, whereas the Mv, Nv and Bv isotope ratios show they were generated from a similar HIMU (table 1) mantle.

In 2005, Bailey et al. reported finding several carbonatite lavas in the Calatrava district. Humphreys et al. (2010) further investigated these findings and their study presented evidence of aragonite, calcite and dolomite inclusions, identified by SEM analysis, in olivine phenocrysts from a leucititic lava flow. They suggested that these olivines crystallized from a carbonated silicate melt at >100 km depth, constrained by the depth of aragonite formation. They concluded that significantly rapid quenching and exhumation prevented the aragonite from transforming into calcite. Their study, however, was challenged by Lustrino et al. (2013), who proposed a different model for the presence of calcite: Ultrabasic lavas incorporated carbonate sediments, inhibiting olivine crystal growth, and giving them a skeletal crystal shape, thus allowing absorbed carbonate inclusions to precipitate calcite within the hollow olivine phenocrysts.

2.2 Mantle end members

The mantle source(s) composition(s) for magmatic rocks are represented by four end-members (Table 1). These are distinguished by the relative abundance of the isotope ratios of Sm/Nd, Rb/Sr and U-Pb-Th. The abbreviation HIMU refers to a mantle source enriched in U and Th relative to Pb. The Pb isotope ratios are also very high, whereas Sr ratios are low and Nd ratios are intermediate. This is generally interpreted to be the result of subducted oceanic crust mixed with seawater and recycled into the mantle. Such compositions are would enrich U and Th and remove Pb in the mantle due to the presence of metasomatic fluids (Rollinson 1994).

Table 1 Mantle end members.

Mantle type	origin	Rb/Sr	⁸⁷ Sr/ ⁸⁶ Sr	Sm/Nd	¹⁴³ Nd/ ¹⁴⁴ Nd	²⁰⁶ Pb/ ²⁰⁴ Pb	²⁰⁸ Pb/ ²⁰⁴ Pb	U-Pb-Th
EM I Enriched mantle I	Lower crust	Low	Low	Low	Low	High	High	U/Pb: Low Th/Pb: Low
EM II Enriched mantle II	Continental/ oceanic crust /sediments	High	High	Low	Low	High	High	U/Pb: Low Th/Pb: Low
DM Depleted Mantle	MORB	Low	Low	High	High	Low		Low U/Pb
HIMU (High μ)	Oceanic crust	Low	Low	Inter- mediate	Inter-mediate	Very high	Very high	U/Pb: High Th/Pb: High

After Rollinson (1994).

3. Field relations, sample collection and sample selection

The geological maps of the area from the Geology and Mining Institute of Spain (1928, 1935, 1985) were used in the field to determine suitable sample locations. The sampling aimed to collect representative specimens from each compositional group. The most suitable sample locations were found on sites that were classified as basalt volcanic (Bv), melilitite volcanic (Mv) and nephelinite volcanic (Nv). Therefore, these are the three compositional groups focused on in this study, from which the sample selection was made.

3.1 Field relations

The eight samples (excluding peridotite sample CH26) described in this study have been selected from 30 sampled outcrops in the area (Figs. 1 & 2). The sample sites are distributed over an area of approximately 900 km² and summarized in Table 2. Nephelinite sample site CH14 and basalt sample site CH13 are located 7 km apart in the NW of the CLV. Basalt sample site CH23, nephelinite sample site CH12 and basalt sample site CH27 are located south of CH13 and CH14, CH27 is the southernmost sampling site in this study, located 8 km south of nephelinite site CH12. Melilitite sample site CH9 lies close to peridotite sample site CH26 in the middle of the field. Nephelinite sample site CH5 and melilitite sample site CH4 are juxtaposed in the easternmost part (see also fig 1B).

3.2 Site description

The volcanic outcrops in the Calatrava district are mainly exploited in quarries (Fig. A, B) or crop out in farmland (Fig. 2C). Some sites represent natural outcrops (Fig. 2D), unspoiled by anthropogenic activity. They are generally distinguished as small hills where lava flows crop out of the surface but some are distinguished by fields with darker soil than the surrounding areas. Quarries that cut through the volcanoes give insight to their stratigraphy. Nearest to the surface, lava flows alternate with ash/tuff layers, and soil layers may also be incorporated high in the stratigraphy. These lava flows are glassy and vesicular, and the rock is friable (Fig. 2A) and cover a more massive core (Fig. 2B). The massive core is fine-grained to glassy with olivine and pyroxene phenocrysts. At some sites, the massive core may also be a lava flow, but these lack vesicles. The rock texture is irregular and flow-like, but is not always distinguishable from a massive core that is similar to an intrusion. Intrusion-like cores (Fig. 2B) have little or no flow-like textures such as alignment of phenocrysts. The rock is massive with aphanitic to glass-like groundmass. Crustal xenoliths are present at all sites. Xenolith sizes vary from pebbles to boulders. All outcrops display alteration to some extent. Secondary mineralisation such as calcite and/or zeolite in vesicles are present in all outcrops. Secondary mineralisation of tourmaline and/or epidote is present in some outcrops.

Quarries

Active quarries, abandoned quarries and road-cuts generally bisect the outer lava flows and/or ash layers, giving easy access to the inner, fresher more massive magmatic core. These samples were collected in situ and contained obvious olivine and/or pyroxene phenocrysts. These sampling areas also display very nice cross sections of the lava flows (Figs. 2A, B, E).

Farmland

The outcrops are mostly occurring as small hills/elevation points in the terrain, and may expose the topmost lava flow. Boulders and pieces of the flow have been incorporated within the soil, and the soil is darker in comparison to the reddish soil of farmlands that are not located on top of volcanoes. Volcanic cobbles to small boulder-sized blocks are scattered in the fields, displaying characteristics of pumice to volcanic bombs mixed with more massive blocks. Thus, good, massive, in situ samples can also be found in these areas. However, whether the units represent lavas or are from the more massive inner part of the volcanic body is not known since the area is disturbed due to farming activity (Fig. 2C).

Outcrops not modified by human activities (“natural” in summary table)

Parts of the lava flows crop out around topographic highs and may be overgrown by vegetation. These have not been altered by excavation or farming. The surfaces are weathered, with much secondary mineralisation, but less altered samples are easy to find (Fig. 2D).

3.2.1 Sample selection

Thirty samples of melilite lava, nepheline lava and basaltic lava were collected in which olivine and/or pyroxene crystals were present. From these, samples were selected for further work on the basis of fresh olivine and pyroxene crystals, a lack of secondary mineralisation and a non-friable nature. Samples with a lot of secondary mineralization and/or very vesicular rocks were discarded. The massive samples generally displayed the freshest olivine and/or pyroxene crystals. Nine samples were selected for thin section and electron microprobe (EMP) analyses. Of these, two basalt, two nephelinite and two melilitite thick sections were appropriate for EMP analysis, as they seemed to display two or more phenocryst generations. Some contained olivine crystals with pronounced iddingsite reaction rims (“rusty” crystals), as well as crystals without this rim, crystals of different size and/or shape, e.g.,- rounded

/angular euhedral and subhedral crystals. Due to budget constraints, only four samples were analysed via EMP.

3.2.2 Secondary mineralization and xenoliths

Secondary minerals include calcite or dolomite and zeolite precipitation in vesicles (Fig. 3A). Calcite and zeolite also occur as streaks within the groundmass. Tourmaline has been identified in a single hand sample only. Iddingsite alteration rims are visible as brown rims around several olivine crystals. Crustal xenoliths of granitic compositions are present in some samples. These mostly contain microcline, other feldspars and quartz (Fig. 3H).

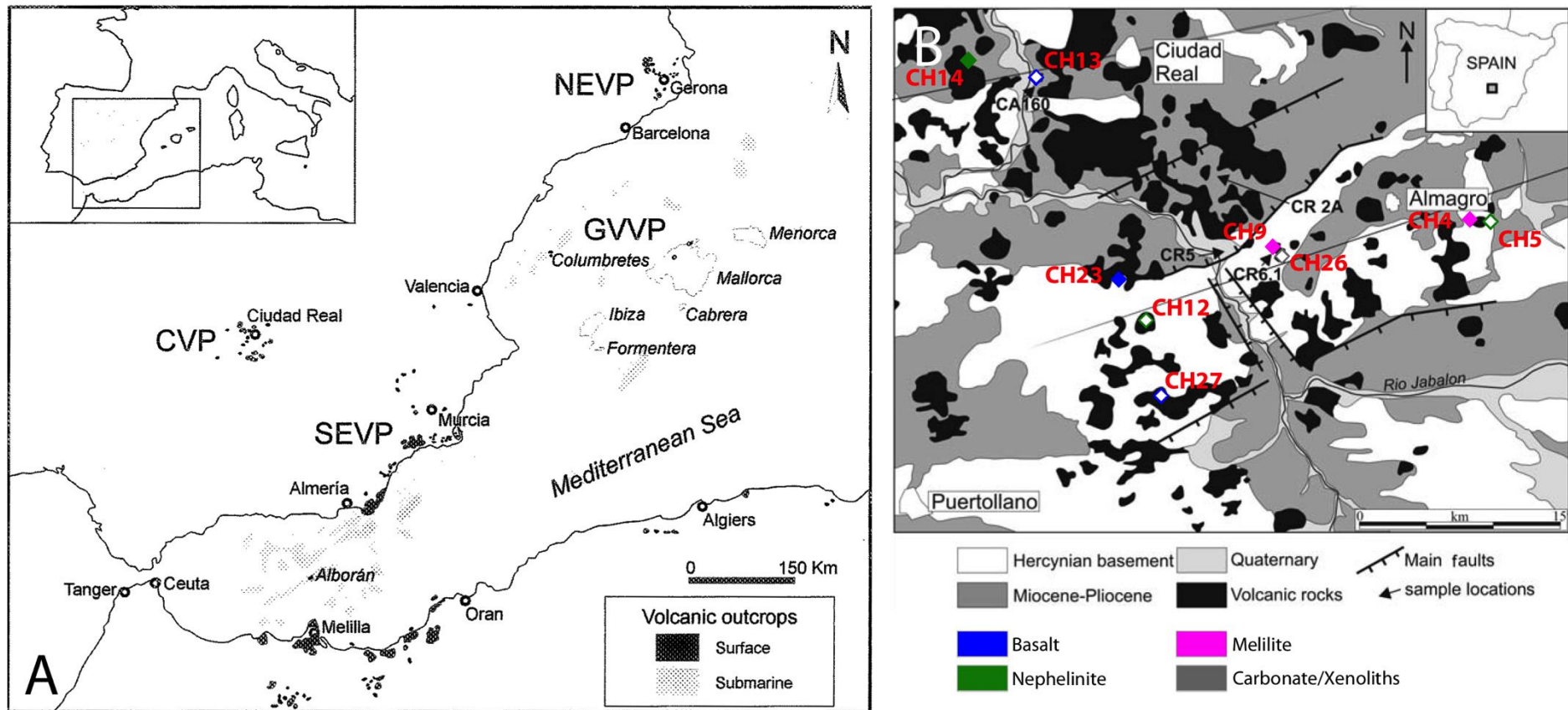


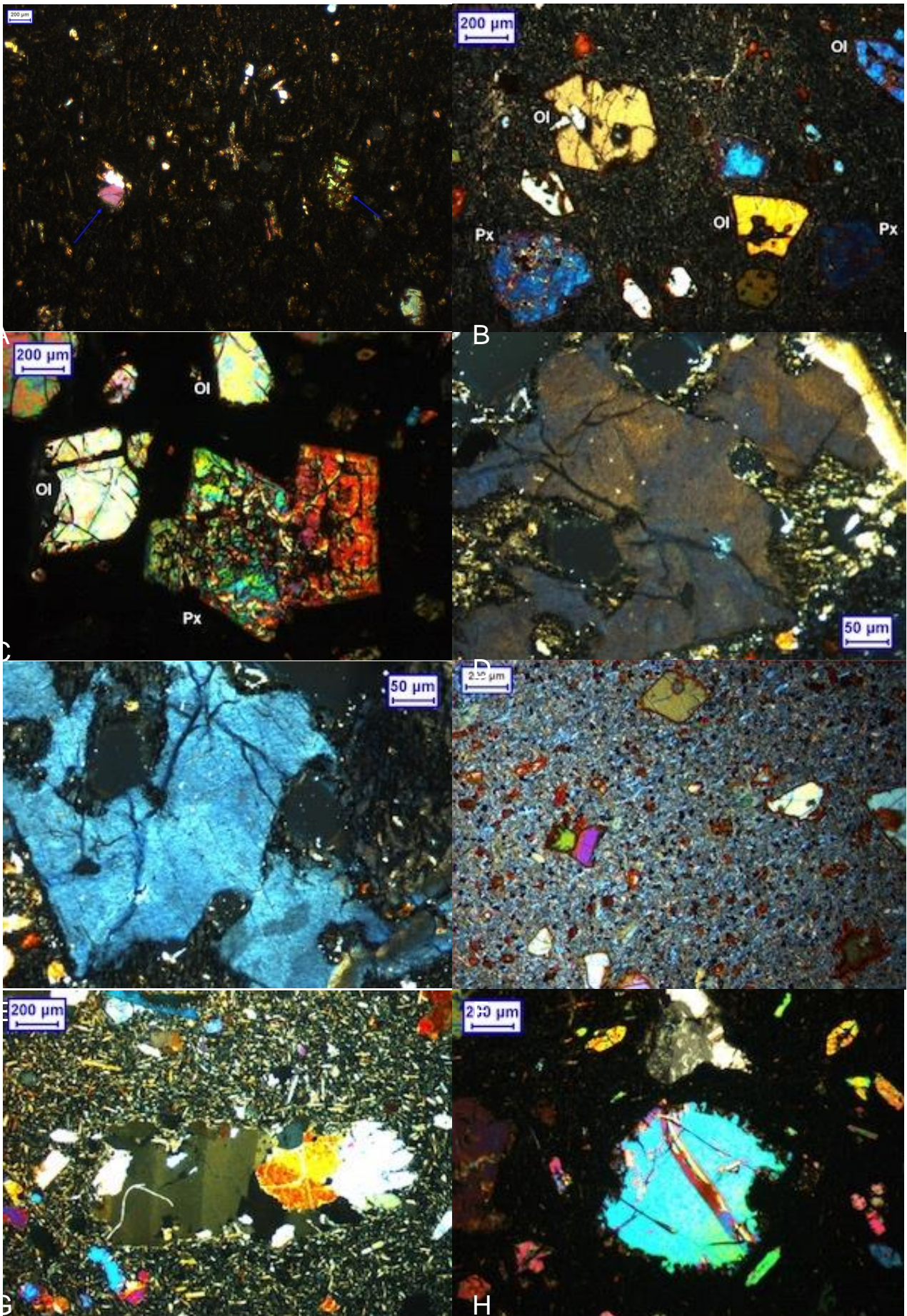
Figure 1. A) Insert of SW Europe with a close-up map of the four Pliocene volcanic outcrops at the Iberian Peninsula, from López-Ruiz et al. 2002. B) Site map, modified from Bailey et. al. (2005). The diamonds with red labels are the samples collected in 2011 and selected for EMP analysis. Filled diamonds are analysed samples, empty diamonds are samples that were not analysed. The sites CH4 and CH5 are mapped as two separate intrusions, one melilite and one nephelinite lava. The samples used in this study were taken on opposite sides of the quarry for diversity. At site CH9, there were three lava outcrops on the top of a hill. One had mostly olivine phenocrysts, one mostly pyroxene phenocrysts and one contained both. CH26 is not a basaltic outcrop. Tuff layers/lava flows comprising a mixture of clasts crop out on the hillside. The clasts seem to be pieces of country rock, peridotite xenoliths and olivine and pyroxene phenocrysts. The arrows with black labels are the sample sites in Bailey et. al. (2005).

Table 2 Site description summary

SITE #	Lava type	Outcrop type	Site description	Lithology description	Phenocrysts; type and diameter	Sample type	Comment	Coordinates lat/long
CH13	Basalt	Farmland	Lava flow on the top of the hill, boulders scattered on farmland	Top of lava flow	Ol, 0,5-1mm in greyish glassy matrix	Boulders	Secondary mineralisation	N: 38°58'5" W: -4°0'19"
CH23	Basalt	Abandoned quarry	Quarry cut through lava flows, nice cross sections	Lava flows on top of massive core	Ol, 0,5-1mm in greyish glassy matrix	Country rock	Secondary mineralisation	N: 38°50'21" W: -3°56'29"
CH27	Basalt	Farmland	Boulders on farmland	Top of lava flow	Ol, 1-2 mm in greyish glassy matrix	Boulder	Olive trees, secondary mineralisation	N: 38°45'20" W: -3°51'40"
CH4	Melilite	Active quarry	Cross sections of lava flows in top of massive core	Ol and px phenocrysts in grey fine-grained/glassy matrix	Ol, px, 0.5-1 cm in greyish glassy matrix	Country rock	In contact with CH5, secondary mineralisation	N: 38°53'16" W: -3°38'54"
CH9	Melilite	Natural	Outcrop located on top of hill Massive country rock	Ol and/or px phenocrysts in brownish fine-grained matrix	Ol, px, 0.5-3 cm, several inclusions visible to naked eye. Carbonate inclusions?	Country rock	Erupted through sedimentary country rock, secondary mineralisation	N: 38°51'5" W: -3°49'2"
CH5	Nephelinite	Active quarry	Cross sections of lava flows in top of massive core	Ol and px phenocrysts in grey fine-grained/glassy matrix	Ol, px, 0.5-1 cm, in greyish glassy matrix. Appear to have more phenocrysts than CH4	Country rock	In contact with CH4, secondary mineralisation	N: 38°53'19" W: -3°38'35"
CH12	Nephelinite	Abandoned quarry	Cinder cone with massive boulders	lapilli, lava flow, massive fine grained boulders with phenocrysts	Ol, 0.5-1 mm in reddish brown glassy matrix	Boulders	Secondary mineralisation	N: 38°48'53" W: -3°54'57"
CH14	Nephelinite	Abandoned quarry	Most of the lava flows removed due to excavation	Lava flow, core, vesicular	Ol, 0,5-1mm in greyish glassy matrix	Country rock	Quarry turned into a garbage dump, secondary mineralisation	N: 38°59'14" W: -4°5'2"
CH26	Peridotite/ Carbonate tuff	Natural	lava flow crops out on side of hill	Tuff/rim breccia, country rock clasts mixed with phenocrysts, xenoliths	Tuff clasts 1-3 cm, ol and px phenocrysts 1-2 mm, peridotite xenoliths 10 cm	Xenolith + lava flow	One of the sites as reported by Bailey, 2005, secondary mineralisation	N: 38°50'17" W: -3°49'25"



Figure 2. **A)** Site CH4, active quarry with melilite volcanic. Outcrop with a massive core. The rock is vesicular, but to a much less extent than the “flow-like” units. The vesicles have calcite/zeolite precipitations, which can be seen close to the geological hammer. **B)** Site CH14, abandoned quarry with nephelinite volcanic. Photo of a massive, “flow-like” core. The basalt is vesicular and friable. The notebook is 10 cm long. **C)** Site CH27, basalt volcanic in farmland outcrop. Volcanic boulders are scattered on the ground. Farmlands like these generally occur on hillsides and do not have a visible natural outcrop on the hilltop. **D)** Site CH9, outcrop of melilite volcanic on the top of a hill. Generally, outcrops like these seem to be excavated but some remain unaffected. **E)** Abandoned quarry with cross sections of ash layers and lava flows



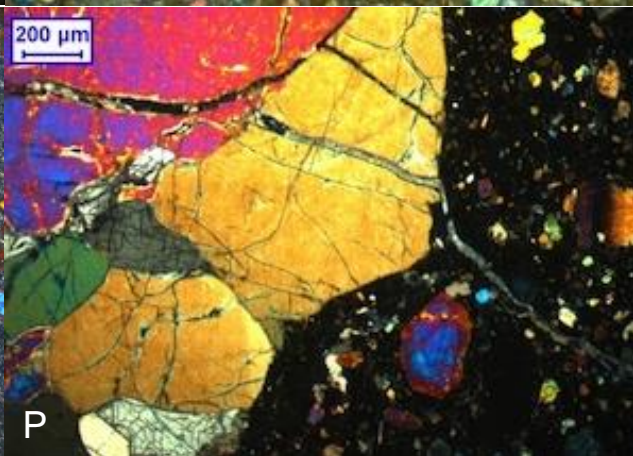
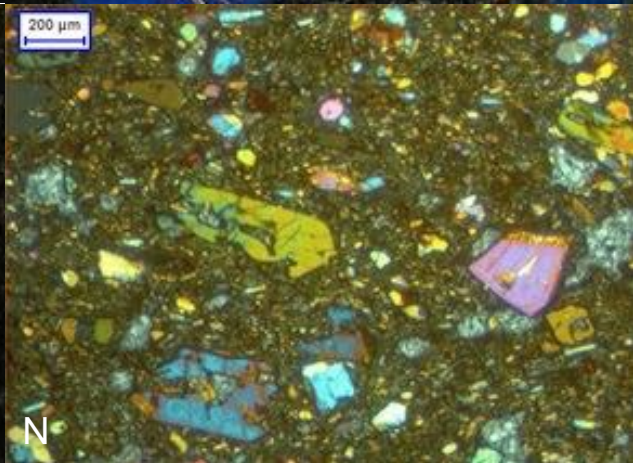
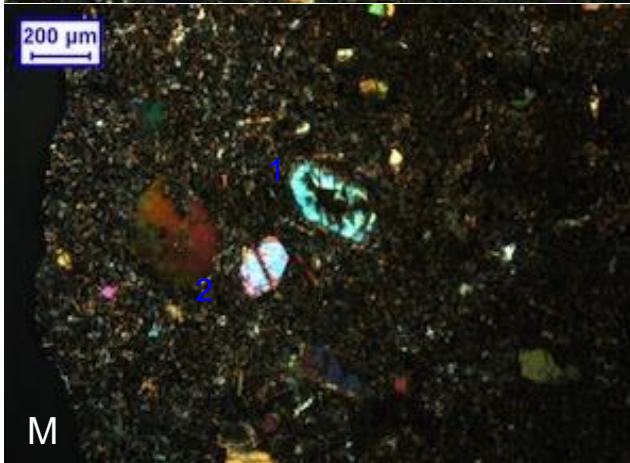
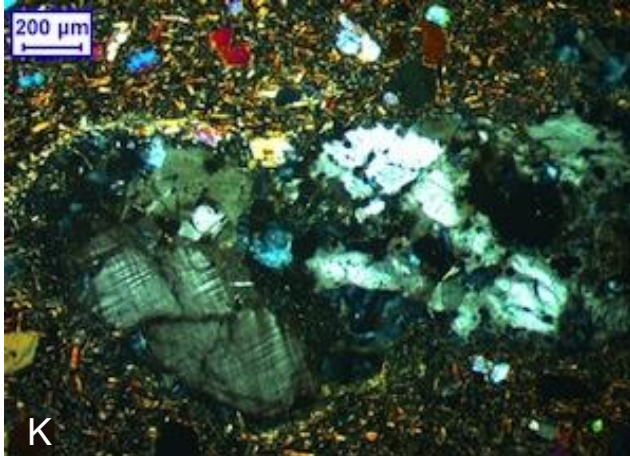
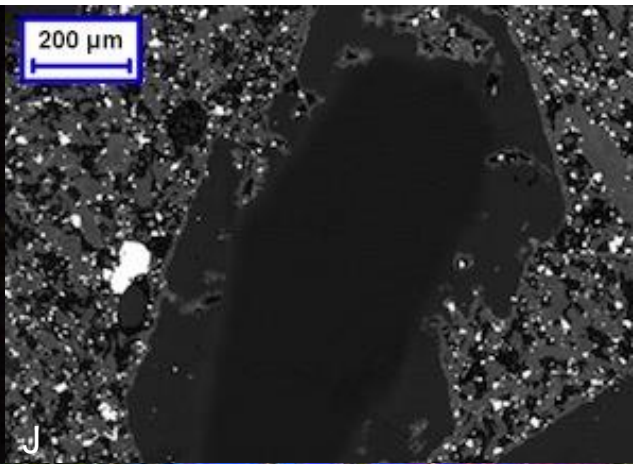
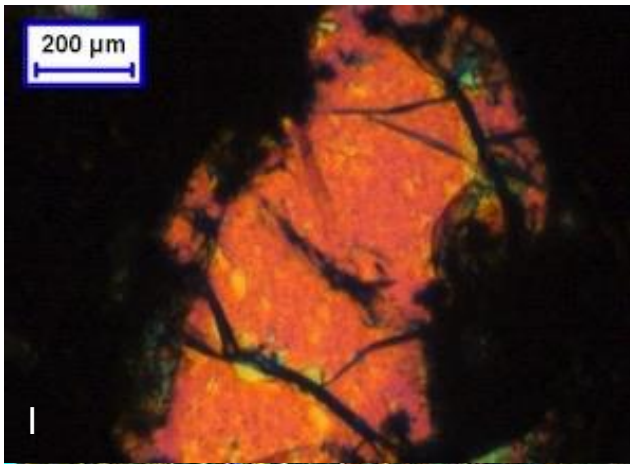


Figure 3. Thick and thin section microphotographs. Thick sections generate a less colourful image. A) Thick section of sample CH13, two olivine phenocrysts in different (?) stages of chemical breakdown. This sample was not analysed due to time constraint. B) Thick section of sample CH23. Olivine and pyroxene crystals. Skeletal olivines with an iddingsite rim giving a “rusty” appearance. The pyroxene crystals show sieve/spongy resorption textures. The pyroxene crystal in the lower right corner is an example of a patchy zoned pyroxene, displayed by the irregular colour alteration. As in sample CH4, the plagioclase laths seem to form a lineation around these crystals (most prominent in the lower left corner). C) Thick section of sample CH23 showing sieve/spongy texture in pyroxene. Normal or reversed zoning is seen towards the crystal edges. D & E) Thin section of sample CH23. Part of a melilite phenocryst, showing the blue-brown zoning in a partially extinct crystal (D) and turned 90° to show the anomalous bright blue birefringence colour of a non-extinct crystal. The bright blue birefringence colour and the blue-brown zoning are very characteristic for melilite crystals (E). F) Thin section of sample CH27, which were not analysed. G) Thin section of sample CH4. Aggregates of strained olivine. The texture is most prominent in the largest crystal shown in the picture, but the feature also occurs in the adjacent extinct and bright crystals. This feature was not prominent in the thick sections. H) Thick section of sample CH4. Olivine crystal with a nucleation rim. Small, elongated olivine crystals (colourful) and plagioclase laths (colourless) seem to form a weak lineation around the large olivine crystal. The grey-white crystals above are calcite or dolomite. I & J) Thick section from sample CH4. Both figures are of the same olivine crystal in cross-polarized light (I) and backscatter electron image (BSE) (J). The compositional difference between core and rim is prominent and shows a distinct nucleation or resorption rim. An example of a “close phenocryst” is seen in the lower right corner. K) Thin section from sample CH4. Crustal xenolith comprised of microcline and quartz. The characteristic microcline twinning is prominent in the lower left side of the image. L) Thin section of sample CH9. Olivine crystal with calcite or dolomite inclusions (high birefringence). M) Thick section of sample CH5 (not analysed). Olivine crystals may belong to separate generations. The crystal (labelled “1”) have a reaction rims and are partially resorbed. It shows typical skeletal crystal form, where the interior has been resorbed. The crystal labelled “2” is euhedral and do not display resorption textures. N) Thin section of sample CH12, which were not analysed. O) Thin section of sample CH14. Olivine phenocrysts in various sizes. A melilite crystal is present in the upper right quadrant and calcite or dolomite precipitations are shown in the lower left quadrant. P) Thin section from sample CH26. A mantle xenolith (left side) with glassy rim (right side). The xenolith is comprised of olivine and pyroxene, which also inhabit the glass rim. An example of a strained olivine crystal can be seen in the middle of the right side of the image.

Table 3 Petrographic summary

SITE #	Lava type	Matrix	Mineralogy	Olivine	Pyroxene	Melilite	Populations	Other
CH 13	Basalt	Fine grained to glassy	Ol, px?	Angular, skeletal, brown "rim" (iddingsite),			2 populations, skeletal vs "rimmed"	
CH 23	Basalt	Glassy	Ol, px, mel	Angular to round, skeletal, elongated to rounded, subhedral with brown "rim" (iddingsite), strained	Patchy zoning, sieve textures, rimmed	Subhedral to rounded, irregular zoning, spongy/sieve textures	2 possible populations, skeletal vs subhedral	
CH 27	Basalt	Fine grained	Ol	Skeletal, resorption textures			all ol have similar appearance	
CH 4	Melilite	Fine grained to glassy	Ol, px, plag in matrix	Skeletal, strained, euhedral to subhedral	Normal and patchy zoning, sieve textures		2 populations? Small vs large	Microcline xenocrysts, secondary zeolite calcite mineralization
CH 9	Melilite	Very fine grained	Ol, px, mel	Elongated, rounded		Subhedral, resorption edges, normal zoning	2 different crystal sizes	Possible melt inclusions, calcite or dolomite inclusions
CH 5	Nephelinite	Fine-grained to glassy	Ol, px, plag?	Resorbed edges, skeletal, angular to round	Patchy zoning, sieve textures		2 populations? Skeletal vs reaction rim	Secondary zeolite calcite mineralization
CH 12	Nephelinite	Fine grained to glassy	Ol	Skeletal, resorption edges			No obvious population difference	
CH 14	Nephelinite	Glassy	Ol, px	Angular, rounded, anhedral, skeletal, brown "rim" brown "rim" (iddingsite), zoning	Patchy zoning, spongy/sieve texture, zoned cpx		2 populations, resorption textures vs less prominent textures	2 cm phenocryst, calcite/carbonate inclusions
CH 26	Carbonatite/xenolith		Ol, px in xenolith, qz, carbonate in tuff	Ol in xenolith are euhedral, ol in tuff are zoned, resorbed	Px in xenolith are euhedral, px in tuff are zoned, resorbed			Peridotite xenolith with glass rim in carbonate tuff

4. Analytical methods

4.1 Petrography

4.1.1 Basalts

CH13 (Fig. 3A)

A few large olivine crystals are present in a very fine grained to glassy matrix. They are 0.5 to 1.5 mm in diameter, are rounded to angular and skeletal, and have iddingsite alteration rims. Crystals about 100 μm in diameter of either pyroxene or olivine are present in the otherwise mostly glassy matrix. These small anhedral crystals have been highly resorbed. In some crystals, zoning can be distinguished. There is no secondary mineralisation visible in thin section, but it is present in hand sample. The small crystals with resorbed textures and the large crystals with reaction rims appear to represent different crystal generations. Therefore this sample was selected for analysis.

CH23 (Fig. 3B, C, D, E)

Crystals of olivine, pyroxene and melilite are present in a glassy matrix. They are angular to round and several have skeletal resorption textures (the crystal's interior is nearly completely broken down). Most of the olivine shows distinct reaction textures. A few crystals are elongated to rounded subhedral crystals with a diameter around 0.5 – 1 mm and an iddingsite alteration rim (Fig. 3B). Strained olivine crystals occur in aggregates. Pyroxene displays disequilibrium patchy zoning and sieve textures (Fig. 3C). Some pyroxene crystals have (or have remnants of) a distinct outer rim with a different composition. Melilite crystals are subhedral, irregularly zoned and have a spongy interior, but have distinct crystal edges (Fig. 3D, 3E). The olivine crystals that are nearly entirely broken down (skeletal and resorbed) and the smaller, subhedral olivine crystals, give the impression that there are two populations present, making this sample suitable for analysis.

CH27 (Fig. 3F)

The sample contains olivine crystals in a fine-grained matrix. Crystal sizes are up to 0.7 mm. All of the olivine crystals, even the groundmass olivine, have an iddingsite alteration rim. The larger crystals are angular to subhedral with various degrees of resorption. Skeletal olivine is

common. The groundmass contains olivine and elongated plagioclase crystals mixed with glass. The similarity of all olivine crystals suggests that they are phenocrysts of a single generation and less interesting for analysis.

4.1.2 Melilitites

CH4 (Fig. 3G, H, I, J, K)

Olivine crystals are rounded to angular crystals in a fine-grained to glassy matrix. The largest crystals are about 1 mm in diameter and the smallest is up to 500 μm in diameter. Most olivine is skeletal euhedral to subhedral with resorbed edges. Some of these only have a thin rim left from the original crystal; the rest of the crystal is altered. Strained olivine crystals appear in aggregates (Fig. 3G). Pyroxenes have a distinct normal zoning as well as patchy zoning and sieve textures. The matrix is fine grained to glassy and the largest crystals in the matrix are plagioclase laths that are about 100 μm long. The matrix displays a weak flow (trachitic) texture defined by plagioclase laths forming an alignment around some olivine crystals, but is not prominent around any other mineral crystals. This is particularly prominent around an olivine phenocryst with a distinct reaction or nucleation rim (Fig. 3H). Melilite is not present in this thin section. Secondary minerals include calcite and zeolite in the matrix and calcite precipitation along fractures in olivine. An aggregate of microcline and quartz with a baked margin are also present (Fig. 3K). The baked margin indicates that this is a crustal xenolith. The differences in crystal size and appearance between large and small crystals may indicate two crystal populations and therefore this section was selected for EMP analysis.

CH9 (Fig. 3L)

Olivine crystals are small (about 1 mm in diameter), elongate (about 1 – 2 cm long), and both rounded and angular. The latter seem to have reaction rims. The large crystals have calcite or dolomite inclusions as well as fine-grained groundmass inclusions, whereas the small rounded crystals have fine-grained groundmass inclusions only. The matrix is very fine grained to glassy with possible melt droplets and/or oxides. Secondary mineralisation of calcite or zeolite occurs in the matrix. Pyroxene and melilite is scarce, but present. The melilite is subhedral with resorbed edges and shows normal zoning without patches or sieve textures. The prominent difference in crystals sizes seem to indicate two populations, one of large

crystals and one of small crystals. Thus this sample was selected for analysis despite the presence secondary minerals.

4.1.3 Nephelinites

CH5 (Fig. 3M)

Olivine crystals are skeletal and angular to rounded. Most of the crystals have resorbed edges, but to differing degrees. There are crystals with very irregular reaction rims and crystals with minor reaction rims. Those with a reaction rim have a less developed skeletal structure. These are all small, 0.5 – 1 mm in diameter. The matrix is fine grained to glassy and the largest of the fine grains are approximately a few microns in size, whereas the rest is a mass of optically unidentifiable crystals and glass droplets. Pyroxene phenocrysts have sieve textures and patchy zoning. Some secondary calcite or zeolite precipitation is also present. The skeletal crystals and the crystals with a very distinct reaction rim may represent two different populations, but due to their fine grain size and the presence of secondary minerals, this section was not prioritized for analysis.

CH12 (Fig. 3N)

Olivine crystals range from 0.1 – 0.5 mm in size and are set in a fine grained to glassy matrix. Olivine crystals <0.1 mm can barely be recognized in the groundmass. Skeletal olivine and resorption occurs more often among the larger crystal population than among the smaller crystal population. There are different crystal sizes but the sample is generally fine grained, thus this sample was not prioritized for analysis.

CH14 (Fig. 3O)

Olivine and pyroxene crystals are set in a fine-grained glassy matrix. The largest phenocryst is a pyroxene 2 cm in diameter with calcite/carbonate inclusions. Other pyroxenes have patchy zoning and spongy textures. Olivine crystals are present and up to 1 cm in diameter. Angular to rounded anhedral/skeletal crystals have brown iddingsite rims that give them a rusty appearance, but a rather homogeneous colour in cross-polarized light. Clinopyroxene crystals are zoned, up to 0.5 mm wide, patchy zoning with sieve texture and a rugged rim. Melilite appears as subhedral rounded phenocrysts with irregular zoning and spongy sieve textures. The matrix is a fine-grained mass of plagioclase laths. Calcite or zeolite precipitation occurs along fractures in the rock. This sample was selected primarily due to two prominent

olivine crystal sizes, those around 0.5 - 1 cm with resorption textures, and smaller crystals with a diameter < 0.5 and less prominent resorption textures.

4.1.4 Carbonate/carbonatite tuff with peridotite xenolith

CH26 (Fig. 3P)

CH26 and CH26-1 are part of a peridotite xenolith found in maar rim deposits (Bailey et al. 2005; Martín-Serrano et al. 2009) and the surrounding tuff. The peridotite contains olivine and pyroxene and the xenolith is rimmed by black glass with phenocrysts of olivine. Single olivine and pyroxene crystals are also found in the deposits surrounding the xenolith. Most of these have glass rims, but a few “free” olivine and pyroxene crystals without glass rims occur. The crystals in the peridotite are very smooth with nice crystal facets, whereas the crystals in the glass rim and the free grains display zoning, reaction rims and resorption textures. The surrounding volcanic tuff deposit consists of clasts 0.5 – 4 cm in diameter containing quartz grains. The quartz crystals display various deformation textures, the most prominent being irregular extinction. The groundmass could be calcite or dolomite, however these are very hard to separate with the optical microscope and should be analysed to determine their chemistry. This sample was not prioritised for analysis, as it was not from any of the lavas originally intended for the study. However the chemistry of the olivine would be an interesting asset for comparing with magma compositions.

4.2 Electron Microprobe

The electron microprobe (EMP) is an instrument that bombards a sample with a focused electron beam. The sample (thin/thick section or similar) is coated with carbon to prevent the sample from becoming electrically charged during the analysis. The sample is put into a sample holder inside a small vacuum chamber in the instrument. Electrons are emitted from a bent tungsten needle with a negative potential. This causes the electrons to accelerate towards the sample. The beam is aimed at a selected area, e.g. a specific mineral grain in a thin section. The atoms within the analytical spot become excited, and as they fall back to their natural state, they generate a spectrum of X-rays specific to each element. The X-ray spectrum is dispersed using a wavelength-dispersive spectrometer and is detected by a proportional counter, which convert the X-rays to energy pulses. The proportional counter is a

small chamber filled with argon gas and contains an anode wire, whereas the chamber walls act as a cathode. When the X-rays hit the argon particles, they are ionised and as the free electrons hit the anode, the energy pulse is created. Thus the energy pulses are proportional to the X-ray wavelength, being constantly generated and counted during the given time frame to establish what elements are within the analytical spot. The beam area can be as small as 1 μm , but a larger diameter is required for most elements. The advantage of EMP analysis is that the method is non-destructive and each analysis is relatively fast, 2-5 minutes. It can be used to chemically classify, map (e.g. zoned crystals) or determine the distribution of ions (e.g. for geothermobarometry) in minerals. EMP instruments that contain argon gas are extremely sensitive to temperature changes, thus it is important to keep the temperature within the room constant (Reed, 2009).

In each thick section, 20-30 olivine crystals were selected for analysis. In samples where apparent phenocrysts and ground mass crystals were both present, 10-15 of each were selected and in samples where there was no distinguishable groundmass olivine, 20-30 crystals were analysed. Quantitative EMP analysis was conducted with a JXA-8530F JEOL Super probe FE-EPMA at the Electron Microprobe Facility, Uppsala University. The running conditions were a 15kV acceleration voltage (HPS), a beam current of 10 nA, a spot size of 1 μm and counting time 2 minutes. The major elements analysed for were SiO_2 , TiO_2 , K_2O , MgO , Al_2O_3 , Na_2O , FeO , MnO and CaO . The calibration standards and a summary of the standard deviations and detection limits for each element are summarised in Table 4 below.

Table 4 Detection limits and standard deviations from EMP analysis

A. Detection Limits of element per sample									
Element	Calibration Standard	Sample							
		CH14	StDev	CH9	StDev	CH23	StDev	CH4	StDev
Si	Wollastonite	103.81	2.01	104.74	2.13	103.91	2.57	104.26	1.98
Ti	Pyrophan (MnTiO ₃)	126.84	7.09	131.43	4.85	130.96	6.36	130.57	7.06
K	Orthoclase	68	3.92	70.54	4.26	69.65	4.04	68.35	5.36
Mg	MgO	75.68	2.6	77.29	2.62	76.35	1.94	77.61	2.15
Al	Al ₂ O ₃	39.87	1.89	39.83	1.64	40.22	2.17	39.78	1.93
Na	Albite	50.71	4.24	50.89	4.11	50.35	4.02	51.74	4.08
Fe	Fe ₂ O ₃	151.74	12.11	151.57	9.16	153.48	11.17	147.48	11.43
Mn	Pyrophan (MnTiO ₃)	120.87	11.72	120.4	10.25	123.83	13.61	126.7	12.45
Ca	Wollastonite	33.45	0.99	33.51	0.85	33.78	1	32.96	1.15

B. Standard deviation of element analysis per sample									
Element	Calibration Standard	Sample							
		CH14	StDev	CH9	StDev	CH23	StDev	CH4	StDev
Si	Wollastonite	0.17	0	0.17	0	0.17	0	0.17	0
Ti	Pyrophan (MnTiO ₃)	86.66	160.25	102.54	176.9	67.87	38.94	194.02	310.93
K	Orthoclase	103.26	106.07	115.61	198.5	97.27	75.51	91.89	36.04
Mg	MgO	0.16	0.01	0.16	0	0.16	0.01	0.16	0
Al	Al ₂ O ₃	38.62	125.91	16.98	6.81	17.15	12.41	21.3	24.11
Na	Albite	66.21	55.65	85.56	112.9	61.67	49.4	190.49	102.68
Fe	Fe ₂ O ₃	0.67	0.04	0.68	0.01	0.65	0.04	0.72	0.04
Mn	Pyrophan (MnTiO ₃)	10.24	2.47	10.96	3.27	13.39	13.87	14.45	7.71
Ca	Wollastonite	2.26	0.23	2.64	0.24	2.25	0.29	2.88	1.56

A) The averaged detection limit for each element in each sample. B. The averaged standard deviation for each element in each sample

4.3 Calculations and modelling

4.3.1 Olivine crystallization

As olivine, $(\text{Mg, Fe})_2\text{SiO}_4$, is often the first mineral to crystallize in a basic magma, olivine crystals preserve an Mg/Fe ratio that reflects its parental magma. Different Mg/Fe ratios in olivine crystals within the same basalt could indicate that the crystals were formed from different parental magmas (Bowen and Schairer 1935, Roeder and Emslie 1970). Olivine forms a solid solution between its two compositional end-members, forsterite (Fo, the Mg end-member) and fayalite (Fa, the Fe end-member). The Fo and Fa content of an Olivine crystal is equivalent to the Mg/Fe content, and the wt.% of FeO and MgO obtained from major element EMP data can be stoichiometrically recalculated to Fo and Fa end member distribution in the olivine formula (Deer et al. 1997).

4.3.2 Distribution coefficient

The distribution (or partition) coefficient, K_D , is used to show how an element behaves between a liquid and a solid. Elements with similar ionic radius and charge will have similar behaviour and may thus substitute for one another in the solid or liquid phase. Different trace elements will have different affinity for the solid phases, thus they will either prefer to go into a solid phase or remain in the residual liquid/melt during cooling and crystallization of a magma body. The distribution coefficient is simply calculated by dividing mole fraction (X) of a component (i) in a solid phase with the mole fraction of the component in a coexisting liquid phase:

$$[1] \quad K_D = \frac{X_i^{\text{solid}}}{X_i^{\text{liquid}}}$$

For trace elements, K_D is obtained by dividing the concentration (C) in the solid phase with the concentration in the liquid phase (Winter 2010):

$$[2] \quad K_D = \frac{C_{\text{Solid}}}{C_{\text{Liquid}}}$$

In this case, the liquid phase is usually represented by glass, i.e.- quenched melt. Magma evolution processes can also be modelled by the fractionation of Fe and Mg in olivine and the melt from which it is crystallized (Roeder and Emslie 1970). If the olivine crystals are in equilibrium with the melt, they will preserve an Mg/Fe ratio that is consistent with the Mg/Fe ratio of the liquid and can be used to calculate the ratio in the melt (Roeder and Emslie 1970, Ulmer 1989, Woronow 1995). The first olivine that crystallizes will have the highest Fo content, e.g. olivine crystals from peridotite (Bowen and Schairer 1935, Roeder and Emslie 1970), and olivine becomes more Fe-rich, i.e.- higher Fa content, as the magma evolves (MacLennan 2003, Ionov 2005, 2005b)

4.3.3 Calculations

The distribution coefficient of MgO and FeO for olivine/liquid has been experimentally determined to = 0.3 (0.26 to 0.36) by Roeder and Emslie (1970) for Mg and Fe between phenocrysts (Ol) and melt (Liq). This fractionation is shown to be independent of temperature. Experiments conducted at a range of temperatures from 1000°C to 1400°C gave a 0.01 variation in K_D . Later experimental studies (Ulmer, 1989) showed that at pressures of 0.1 to 750 MPa (lithospheric mantle depths), K_D varies from 0.29 to 0.31. The formula used to calculate K_D derived by Roeder and Emslie (1970) uses the activities and activity coefficients (previously constrained experimentally by Bowen and Schairer, 1935), as well as the mole fractions (X), for MgO and FeO in melt and phenocrysts, respectively. The formula below is the one used in this study.

$$[3] \quad K_D = \frac{X_{FeO}^{Ol} X_{MgO}^{Liq}}{X_{FeO}^{Liq} X_{MgO}^{Ol}}$$

This formula was used to determine if the olivine crystals are in equilibrium with their host lavas. This was evaluated in two ways: 1) Olivine compositions were compared to host melt compositions using the whole-rock XRF compositions obtained from Cebriá and López-Ruiz (1994, 1996). The average MgO and total FeO (FeO + Fe₂O₃, which in some studies are analysed separately and sometimes analysed as FeO only) data from each rock type were used as X_{MgO}^{Liq} and X_{FeO}^{Liq} . MgO and FeO from olivine EMP analyses were used as X_{MgO}^{Ol} and X_{FeO}^{Ol} . The coefficient required for the crystal chemistry to be in equilibrium with the melt chemistry was calculated for each olivine crystal. K_D values around 0.3 dictates that the crystals are in

equilibrium with the whole-rock composition and that the olivines represent true phenocrysts; values outside the interval 0.29 to 0.31 indicate that the olivine was not in equilibrium with the whole-rock composition and are therefore foreign, xenocrysts, to the host melt. 2) The K_D of 0.3 for olivine-liquid partitioning was used together with the EMP compositional data for X_{FeO}^{Ol} and X_{MgO}^{Ol} to calculate the FeO/MgO ratio of the parent melt in equilibrium with the olivine crystal. Similarly, if the Fo content has been determined, it can be converted to a Fe/Mg ratio for the melt (equation 4; Maclennan et al. 2003).

$$[4] \quad \frac{Fe^{2+}}{Mg} = \frac{1}{K_D} \left(\frac{1-Fo}{Fo} \right)$$

Formula [4] was used to calculate the Fe/Mg ratios of the equilibrium melt, using the Fo (Mg) content of the olivine crystals and assuming a K_D of 0.3 (Fig 5). The Fe/Mg ratios for the respective olivine crystal could thus be compared with whole rock Fe/Mg ratios from Cebriá and López-Ruiz (1994, 1996). To calculate Mg-Fe distribution in a crystal from EMP analyses or in a melt from whole-rock XRF analysis, both Mg# and Fo can be calculated and compared. The Mg number (Mg#) is a differentiation index that determines if a magma (or Mg-Fe bearing minerals in a magma) comes from an ultrabasic, basic or intermediate source with respect to the differentiation between Mg and Fe (Winter 2010). In olivine crystals, the Mg# is used to determine whether an ultrabasic (Mg# > 89) or basic (Mg# < 89) parent melt was involved (Villaseca et al. 2010). Mg and Fe proportions are calculated (equation 5) by dividing wt.% of an oxide (obtained from e.g. XRF or EMP analysis) with the molar weight of the oxide (Winter 2010). Conversion of wt.% oxides into Forsterite-Fayalite fractions was performed according to the method described by Deer et al. (1992) for comparison with Mg#.

$$[5] \quad \frac{Mg}{(Mg + Fe)} \times 100$$

Melt inclusions in olivine crystals represent samples of melt present at the time olivine crystallised. When inclusions are not present, XRF whole-rock compositions can be used to approximate melt compositions (Bédard, 2005). Otherwise fine grained or glassy matrix may be used to approximate the bulk composition of the magma. Jeffries (1995) analysed 50 matrix spots per thin section with laser-ablative inductively coupled plasma mass-spectrometry to determine an average melt composition. Melt inclusions in olivine were not seen in this study and petrographic observations indicated the presence of small crustal

xenoliths and secondary zeolite/calcite precipitation. Consequently, whole-rock XRF analysis of the samples from this study would not represent “pristine” melt, but would reflect contamination. Thus whole-rock compositional analyses from Cebriá and López-Ruiz (1994, 1996) were chosen to represent the melt composition for the different lava types. A limitation of this approach, however, is that the purity of the samples used in the Cebriá and López-Ruiz investigations must be assumed. While carbonatite and zeolite precipitations were described for these samples, no crustal xenocrysts or xenoliths have been reported (Cebriá and López-Ruiz, 1994, 1996). Their whole-rock data was used to obtain the relative Mg/Fe ratios of the olivine phenocrysts and of their parent melt.

5. Mineral Chemistry

5.1 Electron microprobe analytical results

EMP olivine totals should equal 99-100%. The totals from my analytical session varied between 98 and 103 wt.% with an average of 101 wt.%. Thus the results are not publication quality, but they can be used to elaborate on the method proposed in this thesis. There is no obvious correlation between high or low totals and abnormal oxide wt.% and the most common instrumental issues that can result in measurement errors, were monitored during the analyses. Therefore the analytical results have been normalized to 100 % (errors/variations %) and then used for the modelling calculations. Chemical equilibrium between olivine and melt during crystallization (i.e. the parent melt composition, not the host rock composition) is assumed for all calculations. One source of error is that the whole rock compositions used are taken from the literature thus the bulk composition of the sampled lavas in this study may be different than the bulk compositions reported in the literature.

Scans of the thick section are in appendices 10.1 and 10.5 and each thin section has its respective analysis numbered. The analytical points that were removed from the study have not been removed from the scans. CH23 was pre-programmed and left overnight, so the analyses after #31 have not been numbered on the photograph. Mg# calculations are found in appendix 10.2.

5.2 Magnesium numbers

Basalts

Sample CH23 (Table 5, Fig. 4) displays a wide range of Mg# calculated from normalized EMP values. There are three low Mg#-phenocrysts with Mg# = 79.7, 81.0 and 81.9, and a gap to higher Mg# crystals ranging from 83.7 to 87.4.

Melilitites

In sample CH4 (Tables 6 and 7, Fig. 4) the Mg# ranges from 86 to 90.9. Rimmed olivine (Fig. 3H-J) crystals are plotted separately, where the Mg# of cores range from 89.6 to 90 and the rims have a lower Mg# of 85.9 to 87.8. Three of these four rimmed olivine crystals have an adjacent, smaller olivine crystal with the same colour (in BSE imagery) as the rim ; these crystals are also plotted separately as “close phenocryst”, with Mg#s of 87.1, 87.6 and 87.7. The Mg# of the rims and the nearby smaller phenocrysts are consistent with the lower Mg# of the non-rimmed phenocrysts.

Sample CH9 (Table 8 and Fig 4) has the most limited spread in Mg#, ranging from 85.8 to 87.5.

Nephelinites

Sample CH14 (Table 9 and Fig 4) displays a similar range to CH23. Mg# ranges from very low (79.6 and 79.8), to 87.9. There is a gap between the two lowest values and the remainder, which range from 83 to 87.9.

Magnesium numbers calculated from previous work

The Mg# calculated from the whole-rock compositions in Cebriá and López-Ruiz (1994, 1996, see Table 10 and Fig 4) have Mg# from 64.6 to 74.2 for Nv, 63.3 to 76.6 for Mv and 64.4 to 72.2 for Bv.

The Mg# in olivine crystals from mantle xenoliths calculated by Bianchini et al. (2010) range from 84.9 to 89.6 and Mg# in olivine crystals from mantle xenoliths calculated by Villaseca et al. (2010) range from 87-92 and 84.9 to 89.6 (Fig 4).

Table 5 CH23 (basalt)

Section	SiO ₂	TiO ₂	K ₂ O	MgO	Al ₂ O ₃	Na ₂ O	FeO	MnO	CaO	Total	Mg#
CH23	40.570	0.000	0.007	44.668	0.016	0.033	14.205	0.195	0.307	100.000	84.9
CH23	40.687	0.034	0.000	44.949	0.044	0.016	13.888	0.175	0.208	100.000	85.2
CH23	40.354	0.065	0.000	45.362	0.059	0.003	13.872	0.114	0.169	100.000	85.4
CH23	40.959	0.011	0.017	45.981	0.030	0.021	12.629	0.118	0.234	100.000	86.6
CH23	40.664	0.088	0.000	45.996	0.065	0.019	12.805	0.114	0.249	100.000	86.5
CH23	40.501	0.000	0.010	44.980	0.065	0.013	14.021	0.219	0.191	100.000	85.1
CH23	39.930	0.065	0.000	41.887	0.080	0.027	17.550	0.245	0.216	100.000	81.0
CH23	40.403	0.018	0.004	45.175	0.050	0.030	13.939	0.158	0.223	100.000	85.2
CH23	41.162	0.000	0.000	46.431	0.038	0.037	11.888	0.202	0.241	100.000	87.4
CH23	40.144	0.058	0.016	44.036	0.018	0.000	15.240	0.206	0.282	100.000	83.7
CH23	41.161	0.000	0.000	46.528	0.053	0.017	11.963	0.066	0.213	100.000	87.4
CH23	40.387	0.000	0.007	44.985	0.010	0.000	14.238	0.218	0.156	100.000	84.9
CH23	38.398	0.055	0.000	41.941	0.047	0.024	19.100	0.256	0.178	100.000	79.7
CH23	40.440	0.000	0.016	45.134	0.031	0.030	13.995	0.167	0.187	100.000	85.2
CH23	40.869	0.054	0.029	46.168	0.037	0.008	12.512	0.134	0.190	100.000	86.8
CH23	40.231	0.075	0.002	42.472	0.026	0.000	16.716	0.282	0.197	100.000	81.9
CH23	40.956	0.000	0.011	46.319	0.056	0.000	12.430	0.023	0.206	100.000	86.9
CH23	40.704	0.078	0.032	45.695	0.076	0.023	13.053	0.116	0.223	100.000	86.2
CH23	40.718	0.013	0.000	44.698	0.039	0.000	14.130	0.217	0.185	100.000	84.9
CH23	40.385	0.034	0.013	45.020	0.066	0.013	14.106	0.186	0.178	100.000	85.1
CH23	40.727	0.022	0.000	45.270	0.055	0.000	13.619	0.117	0.189	100.000	85.6
CH23	40.952	0.000	0.000	46.266	0.077	0.009	12.286	0.135	0.275	100.000	87.0
CH23	40.659	0.000	0.000	44.992	0.068	0.010	13.915	0.180	0.178	100.000	85.2

Normalized EMP values from analysis of olivine phenocrysts in sample CH23 and Mg# for the phenocrysts

Table 6 CH4 (melilite)

Section	SiO ₂	TiO ₂	K ₂ O	MgO	Al ₂ O ₃	Na ₂ O	FeO	MnO	CaO	Total	Mg#
CH4	40.790	0.000	0.002	46.562	0.056	0.043	12.200	0.141	0.208	100.000	87.2
CH4	41.007	0.044	0.000	47.390	0.059	0.013	11.162	0.122	0.203	100.000	88.3
CH4	40.832	0.000	0.000	47.380	0.033	0.018	11.412	0.163	0.162	100.000	88.1
CH4	40.589	0.000	0.000	45.690	0.063	0.010	13.294	0.152	0.202	100.000	86.0
CH4	40.989	0.061	0.000	46.142	0.056	0.031	12.407	0.168	0.147	100.000	86.9
CH4	41.446	0.006	0.061	47.465	0.018	0.039	10.677	0.100	0.190	100.000	88.8
CH4	41.380	0.082	0.001	47.590	0.050	0.008	10.537	0.131	0.219	100.000	89.0
CH4	41.214	0.012	0.000	47.488	0.042	0.029	10.835	0.151	0.230	100.000	88.7
CH4	40.973	0.059	0.018	47.427	0.077	0.003	11.168	0.113	0.162	100.000	88.3
CH4	41.654	0.063	0.000	49.122	0.032	0.032	8.805	0.132	0.160	100.000	90.9
CH4	40.762	0.070	0.003	47.098	0.108	0.009	11.675	0.028	0.248	100.000	87.8
CH4	40.495	0.000	0.046	46.465	0.025	0.000	12.633	0.164	0.172	100.000	86.8
CH4	40.965	0.000	0.023	46.868	0.058	0.038	11.793	0.071	0.184	100.000	87.6
CH4	41.014	0.000	0.013	47.455	0.037	0.004	11.173	0.105	0.199	100.000	88.3
CH4	40.711	0.097	0.007	47.376	0.040	0.028	11.326	0.158	0.257	100.000	88.2
CH4	41.285	0.000	0.000	48.823	0.005	0.000	9.700	0.129	0.058	100.000	90.0
CH4	41.198	0.078	0.024	48.739	0.016	0.018	9.777	0.089	0.061	100.000	89.9
CH4	40.995	0.047	0.019	47.149	0.059	0.023	11.433	0.060	0.216	100.000	88.0

Table 6 continued

Section	SiO ₂	TiO ₂	K ₂ O	MgO	Al ₂ O ₃	Na ₂ O	FeO	MnO	CaO	Total	Mg#
CH4	40.931	0.000	0.034	47.144	0.072	0.036	11.453	0.113	0.219	100.000	88.0
CH4	41.141	0.045	0.023	47.786	0.084	0.000	10.619	0.134	0.167	100.000	88.9
CH4	40.821	0.093	0.009	46.613	0.115	0.045	12.082	0.038	0.184	100.000	87.3
CH4	41.273	0.000	0.004	47.223	0.067	0.011	11.057	0.208	0.157	100.000	88.4
CH4	41.302	0.022	0.000	48.359	0.046	0.001	10.047	0.080	0.143	100.000	89.6
CH4	40.633	0.061	0.019	45.908	0.075	0.008	12.868	0.210	0.219	100.000	86.4
CH4	40.559	0.038	0.000	46.628	0.023	0.019	12.313	0.218	0.202	100.000	87.1
CH4	40.933	0.037	0.022	47.014	0.039	0.000	11.640	0.111	0.204	100.000	87.8
CH4	40.836	0.000	0.000	46.684	0.017	0.000	11.996	0.249	0.219	100.000	87.4

Normalized EMP values from analysis of olivine phenocrysts in sample CH4 and Mg# for the phenocrysts

Table 7 CH4, rimmed phenocrysts (melilite)

Section	SiO ₂	TiO ₂	K ₂ O	MgO	Al ₂ O ₃	Na ₂ O	FeO	MnO	CaO	Total	Mg#
CH4*	41.356	0.026	0.033	48.709	0.022	0.000	9.674	0.135	0.046	100.000	90.0
CH4**	40.749	0.000	0.041	46.074	0.063	0.000	12.425	0.234	0.414	100.000	86.9
CH4°	41.260	0.095	0.000	46.441	0.010	0.023	11.705	0.239	0.227	100.000	87.6
CH4*	41.267	0.000	0.011	48.769	0.013	0.019	9.731	0.129	0.062	100.000	89.9
CH4**	40.515	0.000	0.000	46.421	0.042	0.026	12.567	0.182	0.247	100.000	86.8
CH4**	40.719	0.004	0.000	46.722	0.013	0.003	12.223	0.100	0.216	100.000	87.2
CH4°	41.136	0.038	0.000	46.642	0.036	0.064	11.650	0.181	0.252	100.000	87.7
CH4*	41.009	0.001	0.000	48.577	0.051	0.025	10.073	0.162	0.102	100.000	89.6
CH4°	41.033	0.000	0.011	46.953	0.029	0.015	11.604	0.144	0.212	100.000	87.8
CH4*	41.439	0.005	0.000	48.591	0.027	0.009	9.785	0.087	0.057	100.000	89.8
CH4**	40.823	0.041	0.032	45.363	0.037	0.042	13.295	0.203	0.165	100.000	85.9
CH4°	41.057	0.058	0.000	46.287	0.041	0.015	12.234	0.112	0.196	100.000	87.1

Normalized EMP data for rimmed phenocryst in CH4, *= analysis of core, ** = analysis of rim, ° = analysis of a nearby phenocryst with similar composition as the rim

Table 8 CH9 (melilite)

Section	SiO ₂	TiO ₂	K ₂ O	MgO	Al ₂ O ₃	Na ₂ O	FeO	MnO	CaO	Total	Mg#
CH9	40.375	0.035	0.000	46.275	0.033	0.003	12.909	0.177	0.193	100.000	86.5
CH9	40.911	0.000	0.001	46.660	0.027	0.040	12.046	0.152	0.163	100.000	87.3
CH9	40.774	0.000	0.017	46.379	0.020	0.038	12.357	0.247	0.168	100.000	87.0
CH9	41.154	0.032	0.010	46.122	0.052	0.000	12.265	0.185	0.180	100.000	87.0
CH9	40.992	0.001	0.000	46.641	0.052	0.020	11.868	0.258	0.168	100.000	87.5
CH9	40.578	0.007	0.000	46.552	0.060	0.000	12.451	0.175	0.177	100.000	87.0
CH9	40.685	0.061	0.007	46.087	0.040	0.018	12.732	0.186	0.185	100.000	86.6
CH9	40.577	0.029	0.000	46.532	0.054	0.032	12.407	0.202	0.166	100.000	87.0
CH9	40.678	0.084	0.014	46.880	0.034	0.003	12.013	0.133	0.161	100.000	87.4
CH9	40.706	0.017	0.000	46.686	0.037	0.000	12.275	0.146	0.134	100.000	87.1
CH9	40.814	0.044	0.000	46.717	0.029	0.053	12.035	0.152	0.155	100.000	87.4
CH9	40.911	0.000	0.003	46.643	0.065	0.009	12.121	0.118	0.131	100.000	87.3
CH9	40.991	0.028	0.000	46.581	0.032	0.011	12.012	0.171	0.175	100.000	87.4
CH9	40.712	0.084	0.033	46.455	0.040	0.001	12.311	0.192	0.172	100.000	87.1
CH9	40.866	0.000	0.017	46.695	0.046	0.000	12.030	0.179	0.167	100.000	87.4
CH9	40.419	0.000	0.024	46.483	0.049	0.024	12.667	0.186	0.146	100.000	86.7

Table 8 continued

CH9	40.577	0.000	0.000	46.521	0.035	0.001	12.496	0.208	0.162	100.000	86.9
CH9	40.837	0.018	0.010	46.496	0.029	0.038	12.209	0.177	0.188	100.000	87.2
CH9	40.665	0.048	0.027	46.676	0.043	0.018	12.156	0.186	0.180	100.000	87.3
CH9	40.518	0.030	0.000	46.532	0.017	0.039	12.503	0.167	0.194	100.000	86.9
CH9	40.809	0.004	0.000	46.497	0.053	0.000	12.365	0.111	0.161	100.000	87.0
CH9	40.743	0.000	0.000	46.794	0.047	0.000	12.172	0.082	0.161	100.000	87.3
CH9	40.855	0.000	0.000	45.541	0.078	0.027	13.184	0.147	0.168	100.000	86.0
CH9	40.444	0.000	0.006	46.100	0.051	0.012	13.109	0.114	0.163	100.000	86.2
CH9	40.952	0.000	0.000	46.439	0.028	0.007	12.232	0.165	0.177	100.000	87.1
CH9	40.681	0.075	0.000	46.718	0.057	0.033	12.168	0.096	0.171	100.000	87.3
CH9	40.377	0.072	0.016	46.607	0.048	0.044	12.565	0.127	0.146	100.000	86.9
CH9	40.890	0.049	0.000	46.644	0.036	0.027	11.989	0.178	0.186	100.000	87.4
CH9	40.623	0.052	0.040	45.783	0.019	0.008	13.165	0.146	0.165	100.000	86.1
CH9	40.757	0.023	0.000	46.697	0.027	0.017	12.237	0.070	0.172	100.000	87.2
CH9	40.896	0.046	0.000	46.624	0.018	0.020	12.066	0.124	0.206	100.000	87.3
CH9	40.046	0.034	0.000	46.866	0.031	0.013	12.639	0.227	0.143	100.000	86.9
CH9	40.714	0.056	0.000	46.661	0.049	0.008	12.231	0.122	0.160	100.000	87.2
CH9	40.942	0.000	0.030	46.473	0.042	0.024	12.236	0.106	0.147	100.000	87.1
CH9	40.739	0.039	0.023	45.465	0.038	0.004	13.379	0.138	0.176	100.000	85.8

Normalised EMP values from analysis of olivine phenocrysts in sample CH9 and Mg# for the phenocrysts

Table 9 CH14, (nephelinite)

Section	SiO ₂	TiO ₂	K ₂ O	MgO	Al ₂ O ₃	Na ₂ O	FeO	MnO	CaO	Total	Mg#
CH 14	40.090	0.000	0.000	44.874	0.068	0.007	14.631	0.150	0.180	100.000	84.5
CH 14	40.286	0.019	0.001	45.650	0.037	0.000	13.665	0.135	0.208	100.000	85.6
CH 14	40.577	0.004	0.000	45.535	0.049	0.014	13.453	0.154	0.215	100.000	83.8
CH 14	41.015	0.000	0.011	46.373	0.046	0.024	12.181	0.166	0.184	100.000	87.2
CH 14	40.297	0.064	0.000	46.894	0.020	0.004	12.385	0.150	0.185	100.000	87.1
CH 14	40.711	0.000	0.023	47.344	0.038	0.000	11.613	0.095	0.175	100.000	87.9
CH 14	40.538	0.002	0.008	47.339	0.039	0.022	11.650	0.225	0.177	100.000	87.9
CH 14	40.978	0.093	0.010	46.956	0.060	0.000	11.547	0.129	0.227	100.000	87.9
CH 14	40.932	0.154	0.000	46.903	0.032	0.032	11.645	0.107	0.195	100.000	87.8
CH 14	40.869	0.034	0.022	46.918	0.011	0.003	11.785	0.149	0.208	100.000	87.6
CH 14	40.787	0.107	0.000	46.460	0.031	0.000	12.212	0.177	0.227	100.000	87.1
CH 14	40.980	0.130	0.041	46.392	0.056	0.013	11.999	0.192	0.197	100.000	87.3
CH 14	40.793	0.070	0.000	45.379	0.091	0.028	13.219	0.240	0.181	100.000	86.0
CH 14	39.818	0.057	0.000	46.765	0.079	0.014	12.914	0.160	0.192	100.000	86.6
CH 14	40.887	0.070	0.000	46.320	0.049	0.000	12.316	0.168	0.189	100.000	87.0
CH 14	40.851	0.055	0.026	46.653	0.043	0.018	11.930	0.204	0.220	100.000	87.5
CH 14	40.838	0.016	0.009	46.029	0.082	0.016	12.643	0.170	0.196	100.000	86.6
CH 14	39.300	0.104	0.000	41.223	0.001	0.055	18.582	0.406	0.330	100.000	79.8
CH 14	40.893	0.000	0.010	46.283	0.048	0.021	12.373	0.194	0.178	100.000	87.0
CH 14	40.491	0.054	0.002	46.551	0.053	0.004	12.499	0.129	0.217	100.000	86.9
CH 14	40.741	0.000	0.002	46.167	0.048	0.006	12.697	0.139	0.199	100.000	86.6
CH 14	40.892	0.107	0.000	46.395	0.028	0.035	12.149	0.184	0.211	100.000	87.2
CH 14	40.117	0.000	0.000	44.506	0.055	0.028	14.917	0.150	0.227	100.000	84.2

Table 9 continued

Section	SiO ₂	TiO ₂	K ₂ O	MgO	Al ₂ O ₃	Na ₂ O	FeO	MnO	CaO	Total	Mg#
CH 14	40.981	0.000	0.018	46.759	0.051	0.056	11.704	0.194	0.238	100.000	87.7
CH 14	39.366	0.030	0.010	41.213	0.057	0.030	18.829	0.263	0.201	100.000	79.6
CH 14	40.776	0.035	0.006	45.523	0.083	0.010	13.219	0.183	0.165	100.000	86.0
CH 14	41.164	0.000	0.010	46.259	0.046	0.033	12.075	0.182	0.232	100.000	87.2
CH 14	40.241	0.018	0.010	43.476	0.044	0.004	15.872	0.144	0.192	100.000	83.0
CH 14	40.694	0.043	0.007	46.853	0.012	0.018	12.068	0.134	0.171	100.000	87.4
CH 14	40.743	0.075	0.046	45.377	0.055	0.008	13.377	0.105	0.213	100.000	85.8
CH 14	40.165	0.077	0.023	45.128	0.021	0.033	14.197	0.128	0.228	100.000	85.0

Normalized EMP values from analysis of olivine phenocrysts in sample CH14 and Mg# for the phenocrysts

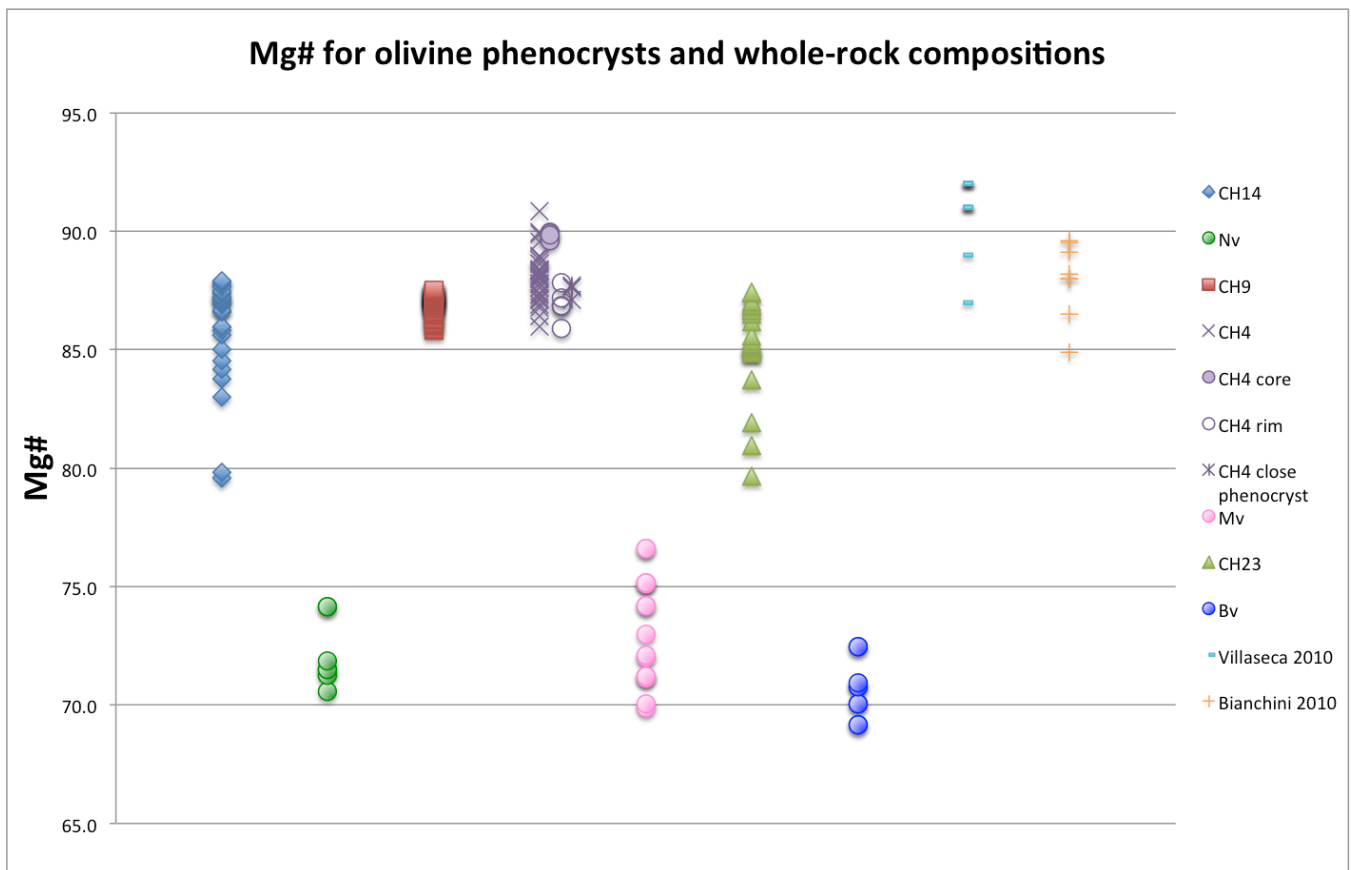


Figure 4 Mg# calculated for all olivine crystals in every sample and for the whole rock compositions of nephelinite, melilitite and basalt, and the Mg# calculated from mantle xenoliths by Bianchini et al. (2010) and Villaseca et. al. (2010). The distribution of the olivine crystals is similar to the distribution in the graph below showing K_D values, but the Mg# of the rock types are lower. It is clear that the Mg# gradually decrease in all samples, implying fractional crystallization, as the melt becomes more enriched in Fe when high Mg olivine crystallize first. In CH4 (purple) there is a prominent difference between the rim and the core in the rimmed olivine crystals, but there are also high Mg# olivine crystals without a rim.

5.3 Distribution coefficients

5.3.1 Distribution coefficients of olivine and whole rock composition

The K_D calculations using whole-rock XRF data from Cebriá and López-Ruiz (1994, 1996) and the EMP analyses of olivine from this study mostly generated values near 0.3; for 17 of crystals in three of the four analysed samples, the K_D values were anomalously lower or higher, as highlighted in red in Table 11.

Basalts

In CH23, K_D varies from 0.27 to 0.52 with an average of 0.33. There are four crystals in the 0.29 to 0.31 range, that could represent true phenocrysts of their basaltic host magma. The crystals that have K_D values <0.29 and >0.31 are not in equilibrium with the basalt whole rock composition. Four crystals have an anomalously high K_D (highlighted in red in table 11).

Melilitite

In CH4, several crystals are apparently in disequilibrium with the melt. The lowest calculated K_D value is 0.20, the highest K_D is 0.33 and the average K_D is 0.27. Low K_D values imply (mathematically) that the required melt needs to be higher in MgO to yield a K_D closer to 0.3. Zoned olivine crystals (Fig. 3H-J) that have high Mg# cores give low K_D (0.23), whereas the rims and the adjacent phenocrysts have K_D 0.28 – 0.33. This implies that the cores initially formed in an environment with much higher MgO content than their rims or the average melilitite composition in the area.

CH9, which is also melilitite, generates the most consistent K_D . The average K_D is 0.3, the lowest being 0.29 and the highest being 0.33. This indicates that the olivine crystals could be true phenocrysts associated with the melilitite.

Nephelinite

Sample CH14 has an average K_D of 0.31 and there are no anomalously low K_D values; thus most olivine crystals represent true phenocrysts from the parent nephelinite. However, there are three anomalously high K_D values, highlighted in red in Table 11. The highest K_D = 0.48. This requires a less primitive (higher FeO content) parental magma and consequently these olivines must be xenocrysts.

Table 10 Whole rock XRF data

Oxide	SiO ₂	TiO ₂	Al ₂ O ₃	Fe ₂ O ₃	FeO	MgO	CaO	Na ₂ O	K ₂ O	P ₂ O ₅	LOI	Total	FeO*	Mg#	
Mv 1996	37.14	2.93	9.98	5.43	6.14	13.83	15.70	3.02	1.51	1.71	2.12	99.71	11.57	74.2	
	40.58	2.93	10.81	4.82	6.17	14.15	13.25	3.11	0.40	0.94	2.40	99.73	10.99	75.2	
	39.80	2.55	9.20	5.80	5.82	15.50	12.28	2.74	1.61	0.95	2.69	99.14	11.62	76.6	
	39.22	2.46	10.80	4.00	7.25	11.78	16.02	3.03	1.58	1.32	1.96	99.61	11.25	69.9	
	39.99	3.18	10.98	6.44	5.76	12.51	13.45	4.46	2.08	0.95	1.42	101.44	12.20	72.0	
	40.12	3.22	10.50	5.08	7.14	13.02	14.23	3.88	1.88	1.18	0.37	100.82	12.22	71.1	
	36.17	3.23	9.72	5.23	7.37	13.49	17.08	2.12	1.19	1.72	1.79	99.33	12.60	71.2	
	39.07	3.15	10.27	4.02	8.02	12.90	14.48	3.33	1.61	1.32	1.40	99.77	12.04	70.1	
	40.25	3.68	11.36	6.90	4.90	12.12	13.59	3.85	2.23	0.93	1.40	100.43	11.80	73.0	
	39.89	3.42	11.08	5.83	5.54	11.83	14.33	3.52	1.45	0.79	2.30	100.19	11.37	72.1	
	1994	36.17	3.23	9.72	5.23	7.37	13.49	17.08	2.12	1.19	1.72	1.79	111.71	12.60	71.2
		37.14	2.93	9.98	5.43	6.14	13.83	15.70	3.02	1.51	1.71	2.12	111.08	11.57	74.2
		39.66	3.58	13.15	5.35	6.86	9.08	12.90	4.78	2.10	1.32	0.51	111.50	12.21	63.6
		39.80	2.55	9.20	5.80	5.82	15.50	12.28	2.74	1.61	0.95	2.69	110.56	11.62	76.6
		40.58	2.93	10.81	4.82	6.17	14.15	13.25	3.11	0.40	0.94	2.40	110.55	10.99	75.2
		40.71	2.83	9.75	4.11	8.01	16.70	10.22	3.78	1.75	1.20	0.69	111.87	12.12	75.1
		39.14	3.05	10.46	5.27	6.53	13.37	14.12	3.29	1.51	1.23	1.75	104.22	11.80	72.6
		Nv 1996	43.96	2.47	11.60	4.57	6.61	12.20	11.25	3.02	1.74	0.46	1.44	99.76	11.18
42.52	2.97		10.88	6.14	5.81	13.81	12.38	4.03	0.74	0.75	1.46	101.66	11.95	74.2	
43.25	0.65		11.83	5.24	6.17	12.22	11.13	5.21	1.08	0.63	1.48	99.07	11.41	71.9	
1994	42.00		2.84	11.94	3.36	7.10	11.58	13.05	3.37	1.51	1.08	1.62	109.91	10.46	70.6
	42.52		2.97	10.88	6.14	5.81	13.81	12.38	4.03	0.74	0.75	1.46	113.44	11.95	74.2
	42.60		3.54	13.12	5.00	6.57	9.03	11.60	3.09	2.24	0.84	2.19	111.39	11.57	64.6
	43.00		3.01	11.40	3.81	6.98	12.10	11.75	3.70	2.11	0.99	1.24	110.88	10.79	71.3
	43.96		2.47	11.60	4.57	6.61	12.20	11.25	3.02	1.74	0.76	1.44	110.80	11.18	71.5
42.98	2.62		11.66	4.85	6.46	12.12	11.85	3.68	1.49	0.78	1.54	107.11	11.31	71.2	
Bv 1996	46.85	2.45	12.30	3.15	7.04	11.10	10.20	2.40	1.71	0.63	1.65	99.64	10.19	70.1	
	46.21	2.15	12.53	3.34	7.40	11.20	10.86	2.62	1.37	0.53	1.24	99.63	10.74	69.2	
	44.90	2.42	12.10	3.91	6.83	11.77	11.15	2.50	1.71	0.68	1.45	99.60	10.74	71.0	
	43.20	2.88	11.00	5.47	5.91	12.36	11.52	2.41	1.02	0.74	3.02	99.71	11.38	72.5	
	43.83	2.78	11.28	4.09	7.50	12.68	12.42	3.30	0.51	0.75	1.65	100.95	11.59	70.8	
	1994	43.20	2.88	11.00	5.47	5.91	12.36	11.52	2.41	1.02	0.74	3.02	110.91	11.38	72.5
		43.83	2.78	11.28	4.09	7.50	12.68	12.42	3.30	0.51	0.75	1.65	112.38	11.59	70.8
		46.21	2.15	12.53	3.34	7.40	11.20	10.86	2.62	1.37	0.53	1.24	110.19	10.74	69.2
		46.75	2.97	13.14	3.60	7.82	9.57	10.55	2.48	1.70	0.66	0.11	110.77	11.42	64.4
		46.85	2.45	12.30	3.15	7.04	11.10	10.20	2.40	1.71	0.63	1.65	109.67	10.19	70.1
	45.18	2.59	11.95	3.96	7.04	11.60	11.17	2.64	1.26	0.66	1.67	105.35	11.00	70.0	

Whole rock XRF analysis of Calatrava igneous rocks from Cebriá and López-Ruíz (1994, 1996). FeO* is total FeO, i.e. FeO + Fe₂O₃. Mg# is calculated with total FeO

Next page: Summary of K_D calculations, using formula [3]. The averaged whole rock XRF composition (with FeO*) for each rock type is used as melt composition. Anomalous K_D - values are highlighted.

Table 11 K_D calculations

Sample	CH14			CH9			CH23			CH4		
	MgO	FeO*	K(d)	MgO	FeO*	K(d)	MgO	FeO*	K(d)	MgO	FeO*	K(d)
melt x	12.119	11.311		13.368	11.798		11.602	10.996		13.368	11.798	
	44.874	14.631	0.35	46.275	12.909	0.32	44.668	14.205	0.34	46.562	12.200	0.30
	45.650	13.665	0.32	46.660	12.046	0.29	44.949	13.888	0.33	47.390	11.162	0.27
	45.535	13.453	0.32	46.379	12.357	0.30	45.362	13.872	0.32	47.380	11.412	0.27
	46.373	12.181	0.28	46.122	12.265	0.30	45.981	12.629	0.29	45.690	13.294	0.33
	46.894	12.385	0.28	46.641	11.868	0.29	45.996	12.805	0.29	46.142	12.407	0.30
	47.344	11.613	0.26	46.552	12.451	0.30	44.980	14.021	0.33	47.465	10.677	0.25
	47.339	11.650	0.26	46.087	12.732	0.31	41.887	17.550	0.44	47.590	10.537	0.25
	46.956	11.547	0.26	46.532	12.407	0.30	45.175	13.939	0.33	47.488	10.835	0.26
	46.903	11.645	0.27	46.880	12.013	0.29	46.431	11.888	0.27	47.427	11.168	0.27
	46.918	11.785	0.27	46.686	12.275	0.30	44.036	15.240	0.37	49.122	8.805	0.20
	46.460	12.212	0.28	46.717	12.035	0.29	46.528	11.963	0.27	47.098	11.675	0.28
	46.392	11.999	0.28	46.643	12.121	0.29	44.985	14.238	0.33	46.465	12.633	0.31
	45.379	13.219	0.31	46.581	12.012	0.29	41.941	19.100	0.48	46.868	11.793	0.29
	46.765	12.914	0.30	46.455	12.311	0.30	45.134	13.995	0.33	47.455	11.173	0.27
	46.320	12.316	0.28	46.695	12.030	0.29	46.168	12.512	0.29	47.376	11.326	0.27
	46.653	11.930	0.27	46.483	12.667	0.31	42.472	16.716	0.42	48.823	9.700	0.23
	46.029	12.643	0.29	46.521	12.496	0.30	46.319	12.430	0.28	48.739	9.777	0.23
	41.223	18.582	0.48	46.496	12.209	0.30	45.695	13.053	0.30	47.149	11.433	0.27
	46.283	12.373	0.29	46.676	12.156	0.30	44.698	14.130	0.33	47.144	11.453	0.28
	46.551	12.499	0.29	46.532	12.503	0.30	45.020	14.106	0.33	47.786	10.619	0.25
	46.167	12.697	0.29	46.497	12.365	0.30	45.270	13.619	0.32	46.613	12.082	0.29
	46.395	12.149	0.28	46.794	12.172	0.29	46.266	12.286	0.28	47.223	11.057	0.27
	44.506	14.917	0.36	45.541	13.184	0.33	44.992	13.915	0.33	48.359	10.047	0.24
	46.759	11.704	0.27	46.100	13.109	0.32				45.908	12.868	0.32
	41.213	18.829	0.49	46.439	12.232	0.30				46.628	12.313	0.30
	45.523	13.219	0.31	46.718	12.168	0.30				47.014	11.640	0.28
	46.259	12.075	0.28	46.607	12.565	0.31				46.684	11.996	0.29
	43.476	15.872	0.39	46.644	11.989	0.29				49.221	9.776	0.23
	46.853	12.068	0.28	45.783	13.165	0.33				46.82	12.626	0.31
	45.377	13.377	0.32	46.697	12.237	0.30				47.186	11.893	0.29
	45.128	14.197	0.34	46.624	12.066	0.29				49.551	9.887	0.23
				46.866	12.639	0.31				47.73	12.921	0.31
				46.661	12.231	0.30				47.598	12.452	0.30
				46.473	12.236	0.30				47.474	11.858	0.28
				45.465	13.379	0.33				49.776	10.322	0.23
										47.563	11.755	0.28
										49.988	10.066	0.23
										46.583	13.653	0.33
										47.091	12.446	0.30
Mean	45.823	13.108	0.308	46.472	12.389	0.302	44.998	14.004	0.330	47.244	11.336	0.273
St dev			0.056			0.011			0.053			0.031

5.3.2. Calculating parental melt compositions

The calculations of parental melt FeO/MgO ratio are summarized in Fig. 5. The calculations using formula [3] are shown in appendix 10.3.

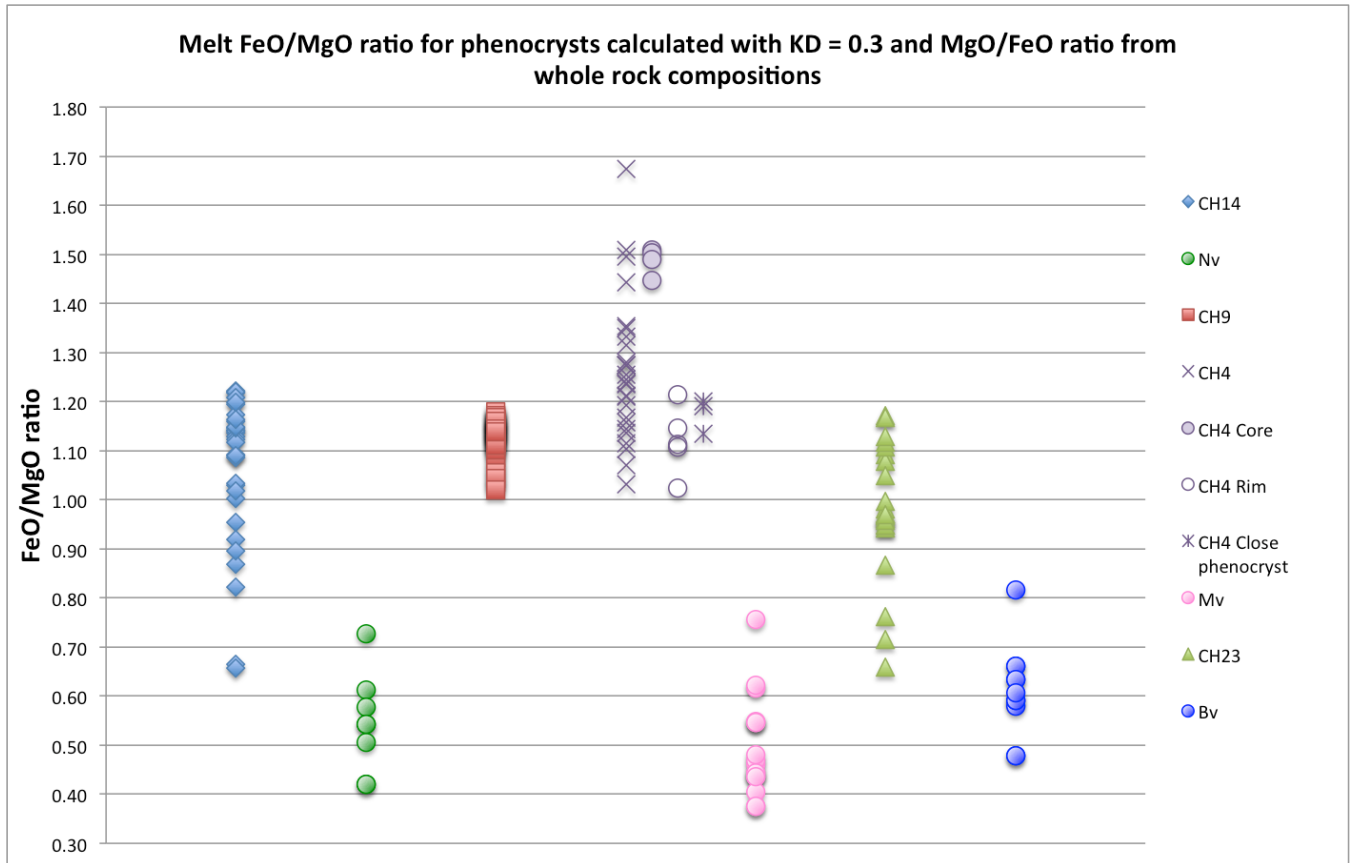


Figure 5 Melt FeO/MgO ratio calculated from EMP olivine compositional data and $K_D = 0.3$, using formula [3], and the FeO/MgO ratios in the whole rock XRF data for each rock type analysed by Cebriá and López-Ruiz (1994, 1996). This reverse modelling of the parent melt shows that the calculated parent melts were generally higher in MgO than the analysed host rocks, thus these olivines represent true xenocrysts. Two crystals in sample CH14 have FeO/MgO ratios close to the measured whole-rock composition of nephelinite, and four crystals in sample CH23 have ratios consistent with the whole rock composition of basalt, suggesting that the olivine in these samples represent true phenocrysts. The olivine crystals in CH4 and CH9 all appear to have formed in an MgO-richer melt than the melilitite whole rock composition and indicating that they represent true xenocrysts.

6. Discussion

6.1 Previous studies

6.1.1 Mantle metasomatism

REE patterns and isotopic signatures in lherzolite and wehrlite xenoliths from the Calatrava district suggest that these originated from an enriched mantle source (EM I, see also table 1) and a radiogenically enriched (HIMU) mantle source, with a greater influence from the HIMU source (Bianchini et al., 2010). A total enrichment in LREE together with enrichment in MREE and depletion in HREE in clinopyroxene indicates pervasive metasomatism, probably by a Fe-Ti-rich HIMU melt or even crystallization directly from the metasomatic agent. There are no metasomatic traces present in the olivine crystals. Isotopic ratios range from 0.70312 – 0.70328 for $^{87}\text{Sr}/^{86}\text{Sr}$, 0.51288 – 0.51295 for $^{143}\text{Nd}/^{144}\text{Nd}$, and 0.28302 – 0.28265 for $^{176}\text{Hf}/^{177}\text{Hf}$ (Bianchini et al., 2010). The same samples have been analysed for $^3\text{He}/^4\text{He}$ and $^{40}\text{Ar}/^{39}\text{Ar}$ isotope ratios (Martelli et al., 2011). High Ar ratios were probably an effect of meteoric contamination, whereas $^3\text{He}/^4\text{He}$ ratios range between 3.6 and 6.5 and are consistent with a HIMU source, supporting metasomatism as an agent with a HIMU isotopic signature (Martelli et al., 2011). Spinel lherzolite xenoliths studied by Villaseca et al. (2010) confirm the mixing of EM with another mantle component, however there is no evidence of Ti-Fe metasomatism. There is enrichment in Th, Pb and U, supporting involvement of a HIMU mantle. Enrichments in LREE and negative Nb-Ta anomalies suggest a subduction-derived component as the metasomatic agent and enrichment in MREE suggests involvement of alkaline silicate melts perhaps mixing with an enriched component that could be recycled oceanic crust (Villaseca et. al 2010).

6.1.2 Melilite-nepheline bearing magmas

Nepheline is a feldspathoid, a silica under saturated mineral, that is common in most alkaline igneous rocks. Intrusive nepheline-bearing magmas crystallize in plutons or as sub-volcanic rocks at medium to shallow crustal depths or as extrusive lavas. Nepheline can form from high-grade metamorphism or metasomatism (nephelinization) of a large variety of protoliths, from syenites and granites to calcite-rich rocks and amphibolites. Occurrence of nephelinites can also be a result of assimilation or contamination of carboniferous sedimentary crust.

Melilite is a Ca-bearing silicate that can occur in both igneous and metamorphic rocks. It crystallizes in impure marbles from the reaction of diopside and calcite. In igneous rocks it can be present in ultramafic plutonic rocks, but is also associated with carbonatites. Melilite in solid solution can form from recrystallization of diopside and nepheline, but at shallow crustal depths with accessible excess H₂O, olivine-melilite-nepheline lavas can form (Deer et al. 1992, 1997).

Melilite and nepheline exist in high Na and/or high K-alkaline igneous rocks. However, the mineral assemblage has also been reported to occur in feldspathoidal rocks as a result of contamination and/or assimilation by carbonate sediments of basaltic magma. (Deer et al. 1992, 1997). Calcite precipitations frequently occur in the samples associated with this study, both at the macro- and microscopic scale. Precipitated calcite and zeolites could indicate abundant excess calcium and carbon in the erupting magma, but it is more likely these precipitations (as well as the secondary epidote mineralisation) are the result of post-magmatic hydrothermal activity and are not a result of crustal contamination and/or assimilation of carbonate sediments.

6.2 Magnesium numbers

The Mg# and Fo/Fa content are both ways to determine how much Mg versus Fe there is in an olivine crystal. These two methods give the same number for Mg and Fo or Fe and Fa content, so studies that use Mg# and studies using Fo content of olivine crystals can be compared directly.

The Mg# (Tables 4-9) of the olivine crystals in this study imply that some of these crystals are formed from more basic magma than their host lavas. Mg# in olivine ≥ 89 indicate an ultrabasic source for the olivine (Villaseca et al. 2010). The Mg# in olivine from lherzolite xenoliths in the Calatrava district vary from 89.2 to 91.5. Wehrlites have Mg# 84.5 to 86 (Villaseca et al. 2010), and Fe-rich lherzolites have Mg# 84.9 to 89.6 (Bianchini et al. 2010). High Mg# olivine (89-91) in melilitite sample CH4 in this study are consistent with crystallization from an ultrabasic source. The source could be the same or similar to the xenoliths reported by Bianchini et al. (2010) and Villaseca et al. (2010) (Fig 3). As a melt evolves down temperature toward a more Fe-rich magma, the Fo content in Olivine crystals will also decrease, decreasing the Mg# and increasing the Fe#.

However, as Villaseca et al. (2010) proposed Fe-Ti-enrichment of a ultrabasic melt, this melt could generate crystals with a lower Mg# but that are still ultrabasic with respect to silica content. Thus the lower Mg# crystals in this study may have been generated as phenocrysts in a low-Mg high-Fe ultrabasic melt. Therefore, the Mg# alone may not be enough to decipher whether olivine phenocrysts are of basic or ultrabasic origin. The phenocrysts cores with Mg# ≥ 89 can be considered to be derived from an ultrabasic parent melt, but it cannot be excluded that compositions with higher Fe content (Mg# < 89) are not from a more Fe-rich ultrabasic source. A similar process has been described by Ionov (2005, 2005b) for low Mg# olivine crystals from mantle xenoliths in the Tok volcanic district in Siberia. In this case recycled oceanic crust melted and infiltrated peridotite, generating the lower-Mg# olivine.

6.3 Olivine distribution coefficient (K_D)

The use of K_D to calculate magma composition from olivine composition is well known (MacLennan 2003), but there are several factors that affect the K_D values between olivine and melt. Roeder and Emslie (1970) stated that the coefficient is 0.3, but the values experimentally obtained in their study vary from 0.26 to 0.36. It could be assumed that the ideal partitioning coefficient for olivine/liquid is 0.3, but values from 0.26 to 0.36 are acceptable. Ulmer (1989) shows a strong correlation ($R = 0.935$) of increasing K_D with increasing pressure. There are however only two measurements made at the highest pressure, which is equal to 255 km depth. At lithospheric depths, the variation is between 0.29 and 0.31. Thus K_D values obtained between olivine crystals and whole-rock compositions from this study, which focuses on melts supposedly derived from the lithospheric mantle, should generate values around 0.3 ± 0.01 . Values that are lower or higher than this indicate that the crystal was not in equilibrium with the melt corresponding to the whole-rock composition, and that the crystal was in equilibrium with a melt composition different from its host.

The olivine crystals (Table 11, Fig. 4) that have K_D values around 0.3 ± 0.01 are assumed to be in equilibrium with the whole-rock composition of their respective host rock. The olivine crystals with anomalous K_D values (highlighted with red in Table 11) are obtained from crystals with much higher Fe-content (see columns for CH14 and CH23 in Table 11), or much lower Fe-content (see column CH4 in Table 11) are interpreted as xenocrysts.

For olivine crystals with higher Mg# (CH4 and CH9) the reverse modelling using olivine MgO-FeO compositions and $K_D = 0.3$ give melt compositions that are more basic than the whole-rock compositions of the host. For the lowest Mg#-crystals in CH14 and CH23, the calculated melt composition correlates well with the whole-rock compositions of Nv and Bv, implying that these crystals could have formed from melts with the same composition as the rocks analysed by Cebriá and López-Ruiz (1994, 1996).

6.4 Crystal petrography and genesis

Disequilibrium features (summarized in Table 3), such as skeletal olivines and resorption features, are present in several crystals. Some of these features are correlated with higher Mg# but there are also crystals with Mg# <89 that show resorption features.

The mineral assemblage observed in the three basalt samples, three nephelinite samples and two melilitite samples all vary within the respective rock type. Lack of rock type-specific minerals such as nepheline in nephelinite does not imply that the nephelinites are incorrectly classified, rather that the mineral may be present (but hard to identify) in the groundmass.

6.4.1 Basalts

Basalt samples contain crystals of olivine and pyroxene (CH13), olivine, pyroxene and melilitite (CH23), and only olivine (CH27). The groundmass in all of these samples is fine-grained to glassy, with no mineral assemblage distinguishable under the microscope. The chemical/normative Alkali olivine basalt classification by Cebriá and López-Ruiz (1994, 1996) requires plagioclase to be present. None of these samples contain visible plagioclase either as megacrysts or in the matrix. Normative classification of whole-rock XRF data would reveal if orthoclase and albite could be equilibrium phases in these rocks.

CH13 (not analysed)

Zoned olivine crystals are a result of changing compositional environment during crystallization. Normal (or reverse) zoning is a result of the changing melt composition as the melt evolves due to crystallization (Streck 2008), and there is no or little influx of more pristine (or evolved) melt. Optically, it is difficult to identify normal or reverse zoning. Resorption textures in olivine on the other hand are easy to recognize and indicate that the crystal begins to dissolve when in disequilibrium with a new melt composition, or due to

temperature changes in the melt (Streck 2008). It is possible to determine that the olivine crystals were formed in one melt and were then mixed, either with evolved magma from the same melt or with another melt. Self-mixing occurs by convection due to temperature differences within one magma body. Mixing with another melt could occur by relocation of the magma body into a chamber containing more evolved melt.

CH23 (analysed)

Sample CH23 contains three olivine crystals with a high Fe content (Fig. 4), thus it is concluded that these were xenocrysts that did not form in their host melt. There is no prominent difference in the resorption textures in relation to their Mg#. This sample has a wide spread in Mg# in olivine crystals, from 79.7 to 89.9. Pyroxene phenocrysts in CH23 show sieve textures, a typical pervasive resorption feature due to a changing chemical environment (Streck, 2008), either due to fractional crystallization or relocation to a magma with a different chemical composition. The optically visible mineral assemblage, olivine + pyroxene + melilite, is the same as melilitite sample CH9, and therefore this sample could be classified as melilitite, or if normative classification shows that nepheline also is an equilibrium phase, this sample can be classified as a melilitite-nepheline bearing basalt.

CH27 (not analysed)

The abundance of skeletal olivine and olivine with resorption features demonstrates that those crystals did not form from the same melt composition as their host rock. This sample was not prioritized for analysis because of the lack of distinctive crystal generations and obvious compositional zoning. However, knowing the chemical composition of the olivine crystals would be useful for determining their origin.

6.4.2 Melilitites

Melilite crystals are visible in melilitite sample CH9, but not in sample CH4. In sample CH9, the mineralogy does not display any strong resorption textures, whereas in sample CH23 there are abundant disequilibrium textures (see Table 3). Sample site CH4 is juxtaposed to nephelinite sample site CH5, which is discussed further below.

CH4 (Analysed)

CH4 contains olivine crystals with Mg#-rich cores = 89.6 to 90, and rims of 85.9 to 87.7. One crystal in Fig. 3I has a core with Mg# 89.9 and rim of 86.8 and 87.2. The rims also show either resorption or nucleation. Another phenocryst in the same thin section (Fig 3H) has a similar Mg#, 90.0, for the core and 86.9 for the rim, but this rim look like a nucleation rim with olivine of a different composition than the host growing along the host crystal edges. Resorption features in olivine crystals result in rounded edges (Streck 2008) so these angular gaps in the crystal structure (Fig. 3I, J) suggest that these rims reflect nucleation. There are also two olivine crystals without rims that have high Mg# (90 and 89.6). The crystals that have Mg# consistent with basic magma, ranging from 86.4 to 88.9, show more or less distinct resorption features or reaction rims. This implies fractional crystallization. As the melt have evolved from ultrabasic to basic and down temperature during crystallization, the crystals that formed first display more prominent resorption features than those crystallizing later. The crystals with high Mg# cores may have formed in a Mg-rich melt, consistent with the high Mg# mantle xenoliths, and later inhabited a more Fe-rich melt. An Fe-enriched rim, Mg# 86.8-87.2, has grown on the xenocrysts and new olivine crystals with higher Fe-content formed (Fig. 3H, I, J). As high-Fe mantle rocks are present in this area, it is not possible to tell if the xenocrysts have existed in a high Fe ultrabasic melt or in an Mg-depleted, basic melt. However, the cores do not show signs of chemical breakdown, as would be expected if the silica content was increasing due to fractional crystallisation as the magma evolves. Olivine crystals formed in an ultrabasic melt will start to dissolve in a basic melt. The optical evidence implies that the silica content must have been the same, only that the melt became Fe-enriched. It might be possible that these rimmed crystals began crystallizing in an ultrabasic melt and were then subjected to mixing with the Fe-Ti enriched metasomatic agent described by Bianchini et al. (2010). As the silica content remained unchanged, the olivine phenocrysts grew rims reflecting the composition of the new melt. To further investigate this, TiO₂ content of rims and cores could be studied using a method with higher detection limit for TiO₂.

The presence of rimmed olivine crystals and remnant xenocrysts with high Mg# mixed with phenocrysts with low Mg# indicate that the chamber beneath this volcano has recharged at least once. The gradual decrease in Mg# in the phenocrysts implies crystal fractionation. The chemical breakdown of the high Mg# phenocrysts suggests that they were mixed into a more

basic melt. The rimmed crystals were mixed into the melt near eruption, as disequilibrium features are not obvious.

CH9 (analysed)

Very narrow reaction rims are distinguished in thin section, but BSE imagery from EMP analysis shows no compositional changes in these, such as those shown for CH4 (Fig. 3H, I). The only distinct differences in the crystal populations is size, and the EMP analyses show that there is little compositional variation (Mg# 86-87). This indicates that these crystals may have formed in a closed system prior to eruption. The location of the volcano is however close to site CH26 (the location described by Bailey et al. 2005). Calcite or dolomite crystals are visible as inclusions in some olivine crystals (Fig. 3L), similar to an olivine phenocryst reported from another site by Humphreys et al. (2010). Optically, it is not possible to determine if these are precipitations, as suggested by Lustrino et al. 2013, or formed at a greater depth, as concluded by Humphreys et al. 2010. Further investigations of these inclusions were ruled out for this study, but could be an interesting future project to either concur or disprove that aragonite crystallized within olivine crystals at mantle depths. The Mg# of olivine phenocrysts reported by Bailey et al. (2005) is 85.2, implying a different origin than the crystals in this study. The Mg# found in olivine crystals at this site in this study is lower than the high-Mg# lherzolites, and more consistent with the high-Fe lherzolites and wehrlites.

An adjacent outcrop (within 50 meters on the same hill, see also table 2, fig 2D) to the one containing only olivine phenocrysts in an aphanitic matrix contains only pyroxene phenocrysts in a similar matrix. Studying these pyroxenes with respect to MgO and FeO content may indicate if their origin is similar to the olivine.

6.4.3 Nephelinites

Nephelinite samples have a variety of phenocrysts but nepheline was not recognized as one of them. As nepheline crystallizes early in alkaline igneous rocks (intrusions or sub-volcanic), it usually forms euhedral crystals (Deer et. al 2004). Nepheline in extrusive rocks occurring in the groundmass matrix can be hard to distinguish optically. No nepheline crystals have been identified in these nephelinite samples. Normative mineralogy of whole-rock chemistry data is needed in order to confirm the rock classification.

CH5 (not analysed)

Sieve textures and patchy zoning are both indicators of disequilibrium crystallization and recrystallization. Change in melt composition can cause the more basic interiors of pyroxene crystals to dissolve. Crystallization of a new composition can be present in the interior voids, or by recrystallization within the crystal lattice to obtain equilibrium with a changed melt composition (Streck 2008). However, there is no BSE imagery of CH5 to identify chemical differences between the rim and the core of these crystals. To determine the crystallization order of the different compositional patches, mapping of the crystal is required, thus it is only possible to conclude for now that patchy zoned pyroxenes have apparently been exposed to changing melt composition. Olivine crystals display similar rims in thin section as CH4. The cores appear intact without signs of resorption, whereas the rims show signs of resorption or nucleation. CH5 is juxtaposed to melilitite sample CH4, which is discussed above.

CH12 (not analysed)

The larger crystals display more prominent resorption than the smaller, groundmass crystals. The larger crystals were able to grow in the melt, but as the melt evolved towards more felsic compositions, these crystals began to dissolve. However, there is no apparent zoning of the olivine crystals to support evolving melt composition during crystallization. BSE imagery could reveal compositional changes that are not visible under the microscope. EMP analysis would reveal if the Mg# in the most resorbed olivine crystals could be resorbed xenocrysts.

CH14 (analysed)

Similar to CH23, high-Fe olivine crystals in sample CH14 also appear resorbed and in disequilibrium with the host rock. Mg# ranges from 79.6 to 87.9. This sample does not contain olivine crystals with Mg# corresponding to an ultrabasic parent melt. Clinopyroxene displays patchy zoning and sieve textures, similar to CH14, showing that these crystals also have been subjected to a changing chemical environment, probably as a result of fractional crystallization or mixing with a melt of a different chemical composition.

6.4.4 Geographical relations

CH4 (analysed) and CH5 (not analysed)

CH5 contains both olivine and pyroxene whereas CH4 contains only olivine. CH5 The similar appearance in thin section of olivine crystals indicate that both these magmas could have been

subjected to mixing with a chemically different melt composition, which is further supported by the patchy zoned pyroxenes. The groundmass in these samples is fine-grained to glassy with possible plagioclase laths present. The samples lack visible melilite or nepheline crystals.

No distinctive contact between the rock types was observed in the field. The proximity of these sites warrants further examination of the chemistry of the pyroxene phenocrysts in sample CH5 to identify the compositions of the mixing agents and to compare with the chemistry of the rimmed olivine crystals in sample CH4. Whole-rock XRF and trace element studies could indicate if the melilitite and nephelinite have the same origin, and whether one of them represents a more pristine melt composition and the other a more evolved composition.

6.4.5 Mineral assemblage

CH23 (analysed) and CH9 (analysed)

Basalt sample site CH23 is located 11 km to the west of melilitite sample site CH9. Both of these samples have the mineral assemblage olivine + pyroxene + melilite, and are the only samples in this study containing optically visible melilite. CH23 has a wide range of Mg# (Fig. 4), whereas sample CH9 defines a narrow range (85.8-87) in Mg# which overlap with the higher Mg# (83.7-86.8) in CH23 (fig 4) thus having crystallized from a melt with a similar MgO/FeO ratio (fig 5).

6.4.6 Presence of high-Fe olivine crystals

CH23 (analysed) and CH14 (analysed)

Nepheline sample site CH14 is located in the northern part of the CLV, 20 km from of basalt sample site CH23, which is located close to the centre of the CLV. The samples from these sites are the most similar in appearance in this study. The analysed olivine crystals display a similar range in Mg# from 79.6 to 87.5 (CH14) and 79.7 to 86.8 (CH23). The Mg# in most olivine crystals range between 83 and 87, but there are two crystals in CH14 and four in CH23 with lower Mg#, from 79.7 to 81.5 (fig 4). These lower crystals also have anomalous K_D (Table 11), and consequently, represent a melt composition with a higher Fe content (Fig 5). Pervasive sieve textures and patchy zoning are present in pyroxene in both samples. Thus, there are implications that early-formed olivine and pyroxene crystals have been subjected to

changing melt compositions. Crystals formed in a primitive melt have been relocated into a more evolved melt, or, a primitive and more evolved melt have been mixed. Partial melting of an Fe-enriched peridotite could generate Fe-enriched basic rocks as the melt evolves. EMP mapping of the patchy zoned pyroxenes crystals in these samples could show if the new melt composition reflected by the zoning is similar to the composition of the high Fe# olivine crystals. Trace element and isotope studies of the olivine and pyroxene crystals could indicate if these crystals bear traces of EM and HIMU or Fe-Ti enriched HIMU, which are the mixing components suggested by Bianchini et al. (2010) and Villaseca et al. (2010).

6.5 Possible evolution of Calatrava field volcanism

Convergence of the African continent towards the Eurasian continent caused compression forming the Alps and extension of the Iberian Peninsula as it was pressed towards SE (Gibbons and Moreno 2002). The rifting generated decompression melting of the mantle wedge beneath the continent and magmas were generated underneath Calatrava (Cebriá and López-Ruiz, 1995, 1996). Ultrabasic magma pooled beneath the crust, allowing cooling and fractional crystallization of the magma. High Mg# olivine and pyroxene crystallised, and accumulated at the bottom of the chamber. The melt differentiated and olivine crystals with higher Fe-content crystallized. The Olivine and pyroxene that had crystallized directly from the basic melt began to dissolve as the new melt composition became higher in silica.

When the magma erupted, the ultrabasic xenoliths, the phenocrysts and xenocrysts of olivine, pyroxene, melilite and nepheline and the now basaltic melt also tore pieces of the crust while making its way to the surface. The erupting lava thus held a mixture of evolved, porphyritic basaltic lava, xenoliths of peridotite origin and crustal origin. The eruptions were explosive, as the magma mixed with ground water on the way to the surface. Ash layers, lapilli and volcanic bombs can be found in crosscuts of the volcanoes and there are several maar craters in the area.

Beneath the continent, eclogite (high-pressure metamorphic basalt) began to melt (Bianchini et al, 2010, Villaseca et al., 2010). The melts were rich in Fe, causing Fe enrichment of the ultrabasic melt. The melts were still ultrabasic with respect to silica content, but some olivine phenocrysts that had begun to crystallize from the melt before mixing, now began to grow

rims enriched in Fe. These phenocrysts, and high-Fe peridotite xenoliths, mixed with the previous melts as the magma chambers were recharged.

7. Conclusions

7.1 Analysed samples

The samples from CH4 (melilitite), CH14 (nephelinite) and CH23 (basalt) contain crystals of variable compositions, showing different disequilibrium features. The compositional range (Fig. 4) supports fractional crystallization. Compositional and petrographic evidence indicate that some crystals are olivine xenocrysts formed in an ultrabasic magma, whereas others phenocrysts have formed in an Fe-enriched magma. The Fe-enriched magma may have been more evolved basalt, or Fe-Ti enriched peridotite. The xenocrysts were transported to, or mixed with, a more evolved magma. Low Mg# phenocrysts may have crystallised in equilibrium with the more evolved melt which hosts them, as melt calculations using the average olivine K_D of 0.3 yield the same FeO/MgO content as the whole rock XRF analysis of nephelinite and basaltic lava.

Crystals in melilitite sample CH9 show the least variation in Mg# and no prominent disequilibrium features. Resorption of the interior has occurred to a lesser degree, allowing calcite to precipitate within the olivine crystals. The olivine Mg#s are equivalent to the Mg# of a basic magma, thus it is likely that these are phenocrysts formed in their host rock and that the host rock composition is not the same as the melilitite whole-rock composition from Cebriá and López-Ruiz (1994, 1996).

7.2 Non-analysed samples

All of the samples that were not analysed in this study display petrographic evidence of changing melt composition during crystallisation. Resorption of olivine phenocrysts in basalt sample CH13 and CH27 and nephelinite sample CH12 show that the melt evolved during the crystallisation causing the earliest formed phenocrysts to begin to dissolve. Nephelinite sample CH5 resembles nephelinite sample CH14 and basalt sample CH23, containing olivine with resorption and sieve textures, and patchy zoning of pyroxene. Nephelinite sample CH5 is

the sample most interesting for further EMP analysis due to the proximity to melilitite sample site CH4 and olivine crystals with similar rims as the zoned olivine xenocrysts in CH4.

7.3 Further studies

Future studies of the rocks at Calatrava would benefit from dating the mantle xenoliths studied by Bianchini et al. (2010) that have evidence of metasomatism. The samples of Villaseca et al. (2010), which do not show such evidence of metasomatism, also need dating in order to see which xenoliths are the oldest. Further studies of calcite within olivine crystals and comparison of these with the calcite precipitations found in several of the rocks could clarify if they have a mantle origin or represent contamination by carbonate sediments. The samples used in this study could be examined more thoroughly, and the techniques used to further quantify the results by analysing the remaining samples and to see if there are more crystals exhibiting the characteristics found here.

The samples that were not prioritized for EMP analysis display features indicating disequilibrium between the crystal and the host melt. EMP analyses of these samples might still be useful for determining parent melt compositions. BSE imagery may also, as in melilitite sample CH4, reveal compositional changes that are not visible under the microscope and provide potential EMP targets.

Groundmass analyses should also be done to get more accurate whole-rock compositions. Normative classifications of groundmass data would illuminate the mineral phases that may not be visible under the microscope to determine if the current classifications are correct.

8. Acknowledgements

My greatest acknowledgement goes to my supervisor Victoria Pease for all the support I have received during this project. I also acknowledge Aitor Cambeses Torres, my field assistant and interpreter in Spain, Jane Scarrow at the University of Granada, for supervision in Spain and helpful comments on the text, and Hans Harryson at Uppsala University for performing EMP analysis and letting me run analyses overnight. I also want to thank all my friends, colleagues and fellow course mates from the Department of Geological Sciences at

Stockholm University through the years. At last but not the least, I thank my parents and Romain for their comfort and support.

9. References

- Ábalos, B.** Carreras, J. Druguet, E. Escuder-Viruete, J. Gómez- Pugnare, M. T. Alvarez, S. L. Quesada, C. Rodríguez-Fernández, L. R. Gil-Ibarguchi, J. I. 2002 *Chapter 9 Variscan and Pre-Variscan Tectonics Geology of Spain*, The Geological Society of London, p 155-183
- Bailey, K.** Garson, M. Kearns, S. & Velasco, A.P. 2005 *Carbonate volcanism in Calatrava, central Spain: a report on the initial findings* Mineralogical Magazine, vol 60 (6), pp 907-915
- Bédard, J.H.** 2005 Partitioning coefficients between olivine and silicate melts *Lithos*, vol 83; p 294-419
- Bianchini, G.** Beccaluva, L., Bonadiman, C., Nowell, G. M., Pearson, D. G., Siena, F. & Wilson, M. 2010 *Mantle metasomatism by melts of HIMU piclogite components: new insights from Fe-lherzolite xenoliths (Calatrava Volcanic District, central Spain). Petrological Evolution of the European Lithospheric Mantle*, Geological Society, London, Special Publications, 337, pp 107 – 124.
- Bowen, N. L.** Schairer, J. F. 1935 *The system MgO-FeO-SiO₂*. American Journal of Science vol 29; p 151-217
- Cebriá, J.M.** López-Ruiz, J. 1995 *Alkali basalts and leucitites in an extensional intrac ontinental plate setting: the late Cenozoic Calatraca Volcanic Province (central Spain)* *Lithos*, vol 36; p 27-46
- Cebriá, J.M.** López-Ruiz, J. 1996 *A refined method for trace element modelling of nonmodal batch partial melting processes: The Cenozoic continental volcanism of Calatrava, central Spain* *Geochimica et Cosmochimica Acta*, Vol. 60; No. 8; pp. 1355-1366
- Cebriá, J.M.** Martín-Escorza C. ,López-Ruiz J. Morán-Zenteno D.J. Martiny B.M. 2011 *Numerical recognition of alignments in monogenetic volcanic areas: Examples from the Michoacán-Guanajuato Volcanic Field in Mexico and Calatrava in Spain* *Journal of Volcanology and Geothermal Research*, vol 201; p 73–82
- Colmenero, J.R.** Fernandez, L.P. Moreno, C. Bahamonde, J.R. Barba, P. Heredia, N. González, F. 2002 *Chapter 6 Carboniferous Geology of Spain*, The Geological Society of London, p 93-116
- Coltorti, M.** Downes, H. Grégoire, M. & O’Rielly, S.Y. 2010 *Petrological evolution of the Europa lithospheric mantle: introduction* Geological Society, London Special Publications; v 337; p 1-5
- Gibbons, W.** & Moreno, T. 2002 *Introduction and overview Geology of Spain*, The Geological Society of London, p 1-6
- Gibson, S. A.** Malarkey, J. Day, J.A. 2008 *Melt Depletion and Enrichment beneath the Western Kaapvaal Craton: Evidence from Finsch Peridotite Xenoliths* *Journal of Petrology* vol 49 no 10, p 1817-1852
- Helz, R.T.** 1987 *Diverse olivine types in lava of the 1959 eruption of Kilauea volcano and their bearing on eruption dynamics* In: *Volcanism in Hawaii*. Decker RW, Wright TL, Stauffer PH (eds) US Prof Paper
- Deer, W.A.** Howie, R. A. Zussmann, J. 1992 *An introducton to rock-forming minerals, second edition* Pearson Prentice hall, Edinburgh gate, Harlow, England 1992
- Deer, W.A.** Howie, R. A. Zussmann, J. 1997 *An introducton to rock-forming minerals, vol 1B, disilicates and ring silicates, second edition* The Geological Society Publishing house, London 1997
- Deer, W.A.** Howie, R. A. Zussmann, J. 2004 *Rock-forming minerals, vol 4B, Framework silicates Silica*

minerals, Feldspathoids and the Zeolites, second edition The Geological Society Publishing house, London 2004

Humphreys, E. R. Bailey, K. Hawkesworth, C.J. Wall, F. Najroka, J. & Rankin, A.H. 2010 *Aragonite in olivine from Calatrava, Spain – Evidence for mantle carbonatite melts from >100 km depth* *Geology*, vol 38; p 911-914

Ionov, D. A. Chanefo, I. Bodinier, J.L. 2005, *Origin of Fe-rich lherzolites and wehrlites from Tok, SE Siberia by reactive melt percolation in refractive mantle peridotites* *Contributions to Mineralogy and Petrology* vol 150; p 335-353

Ionov, D. A. Prikhodko, V. S. Bodinier, J.L. Sobolev, A. V. Weis, D 2005b *Lithospheric mantle beneath the south-eastern Siberian craton: petrology of peridotite xenoliths in basalts from the Tokinsky Stanovik.* *Contributions to Mineralogy and Petrology* vol 149; p 674-665

Instituto Geológico y Minero de España, 1928 *Mapa Geológico de España* [electronic] Almodóvar del Campo (Norte de Puertollano) 810, 18-32 Series 1ª 1:50000 Instituto Geológico y Minero de España, Madrid 1928 (<http://info.igme.es/cartografia/geo50.asp?hoja=810&bis>)

Instituto Geológico y Minero de España, 1934 *Mapa Geológico de España* [electronic] Moral de Calatrava 811, 19-32 Series 1ª 1:50000 Instituto Geológico y Minero de España, Madrid 1934 (<http://info.igme.es/cartografia/geo50.asp?hoja=811&bis>)

Instituto Geológico y Minero de España, 1985 *Mapa Geológico de España* [electronic] Ciudad Real 784, 18-31, Series 2ª, 1:50000 Madrid Raycar, S. A. Impresores (<http://info.igme.es/cartografia/magna50.asp?hoja=784&bis>)

Instituto Geológico y Minero de España, 1985 *Mapa Geológico de España* [electronic] Almagro 785 19-31 Series 2ª 1:50000 Madrid Raycar, S. A. impresores (<http://info.igme.es/cartografia/magna50.asp?hoja=785&bis>)

Jeffries, T.E Perkind, W.T. Pearce, N.J.G. 1995 *Measurements of trace elements in basalts and their phenocrysts by laser probe microanalysis inductively coupled plasma mass spectrometry (LPMA-ICP-MS)* *chemical Geology* 121; 131-144

López-Gómez, J. Archie, A. Pérez-López, A. 2002 *Chapter 10 Permian and Triassic Geology of Spain*, The Geological Society of London, p 185-212

López-Ruiz, J. Cebriá, J.M. Doblas, M. 2002 *Chapter 17 Cenozoic volcanism I: the Iberian Peninsula Geology of Spain*, The Geological Society of London, p 417 – 438

Lustrino, M. Agostini, S. Capizzi, L.S. Psarakis, M. & Prelević, D. 2013 *Carbonate, not carbonatite, at Villamayor volcano (Calatrava Volcanic District, Central Spain)* *Goldschmidt 2013 abstracts*

MacLennan, J. McKenzie, D. Grönvold, K. Shimizu, N. Eiler, J.M.Kitchen, N. *Melt mixing and crystallization under Theistareykir, northeast Iceland Geochemistry*, *Geophysics, Geosystems (G³)*, vol 4, No 11, art 8624

Martín-Serrano, A. Vegas, J. García-Cortés, A. Galán, L. Gallardo-Millán, J.L., Martín Alfageme, S. Rubio, F.M. Ibarra, P.I. Granda, A. Pérez-González, A. & García-Lobon, J.L. 2009 *Morphotectonic setting of maar lakes in the Campo de Calatrava Volcanic Field (Central Spain, SW Europe)* *Sedimentary Geology*, vol 222, p 52-63

Martelli, M Bianchini, G., Beccaluva L, Rizzo, A 2011 *Helium and argon isotopic compositions of mantle xenoliths from Tallante and Calatrava, Spain* Journal of Volcanology and Geothermal Research 200, 18–26

Reed, S.J.B. 2009 *Electron Microprobe analysis and Scanning Electron Microscopy in geology, second edition* University of Cambridge online publication 2009 (<http://dx.doi.org/10.1017/CBO9780511610561>)

Roeder P.L & Emslie R.F 1970 *Olivine-Liquid equilibrium* Contributions to Mineralogy and Petrology 29, 275-289

Rollinson, H. 1993 *Using geochemical data: Evaluation, presentation, interpretation* Pearson Education Limited, 1993

Streck, M.J. 2008 *Mineral Textures and Zoning as Evidence of Open System Processes* Mineralogy & Geochemistry; vol 69; pp. 595-622.

Ulmer, P. 1989 *The dependence of the Fe²⁺-Mg cation-partitioning between olivine and basaltic liquid on pressure, temperature and composition An experimental study to 30 kbars* [Contributions to Mineralogy and Petrology](#), Volume 101, [Issue 3](#), pp 261-273

Valladares, M. I. Barba, P. Ugidos, J. M, 2002 *Chapter 2 Precambrian Geology of Spain*, The Geological Society of London, p 7-16

Villaseca, C. Ancochea, E. Orejana & Jeffries, T.E. 2010 *Composition and evolution of the lithospheric mantle in central Spain: inferences from peridotite xenoliths from the Cenozoic Calatrava volcanic field* Geological Society, London Special Publications; v 337; p. 125-151

Winter, J.D. 2010 *Principles of igneous and metamorphic petrology, Second edition*, Pearson Prentice Hall, Upper Saddle River New Jersey 2010

Woronow, A. Reid, A. M. Jones, J.H. 1995 *Parental magma compositions inferred from the chemical compositing of olivine-controlled derivative melts* *Geochemica et Cosmochemica Acta*, vol 60 No 4 p 577-586

10. Appendices

10.1 Original EMP data

CH23 – Basalt

Oxide	SiO ₂	TiO ₂	K ₂ O	MgO	Al ₂ O ₃	Na ₂ O	FeO	MnO	CaO	Total
	41.048	0	0.007	45.194	0.016	0.033	14.372	0.197	0.311	101.178
	41.252	0.034	0	45.573	0.045	0.016	14.081	0.177	0.211	101.389
	41.442	0.067	0	46.585	0.061	0.003	14.246	0.117	0.174	102.695
	41.240	0.011	0.017	46.296	0.030	0.021	12.716	0.119	0.236	100.686
	40.904	0.089	0	46.267	0.065	0.019	12.880	0.115	0.250	100.589
	41.066	0	0.01	45.608	0.066	0.013	14.217	0.222	0.194	101.396
	40.014	0.065	0	41.975	0.080	0.027	17.587	0.246	0.216	100.210
	41.258	0.018	0.004	46.131	0.051	0.031	14.234	0.161	0.228	102.116
	41.281	0	0	46.565	0.038	0.037	11.922	0.203	0.242	100.288
	41.221	0.06	0.016	45.217	0.018	0	15.649	0.212	0.290	102.683
	41.421	0	0	46.822	0.053	0.017	12.038	0.066	0.214	100.631
	40.597	0	0.007	45.219	0.010	0	14.312	0.219	0.157	100.521
	37.897	0.054	0	41.393	0.046	0.024	18.851	0.253	0.176	98.694
	41.388	0	0.016	46.192	0.032	0.031	14.323	0.171	0.191	102.344
	41.586	0.055	0.029	46.978	0.038	0.008	12.731	0.136	0.193	101.754
	40.699	0.076	0.002	42.966	0.026	0	16.910	0.285	0.199	101.163
	41.025	0	0.011	46.397	0.056	0	12.451	0.023	0.206	100.169
	40.611	0.078	0.032	45.591	0.076	0.023	13.023	0.116	0.222	99.772
	41.080	0.013	0	45.096	0.039	0	14.256	0.219	0.187	100.89
	41.676	0.035	0.013	46.459	0.068	0.013	14.557	0.192	0.184	103.197
	41.339	0.022	0	45.950	0.056	0	13.824	0.119	0.192	101.502
	41.584	0	0	46.980	0.078	0.009	12.476	0.137	0.279	101.543
	41.224	0	0	45.617	0.069	0.010	14.108	0.182	0.180	101.390

CH4 – Melilitite

Oxide	SiO ₂	TiO ₂	K ₂ O	MgO	Al ₂ O ₃	Na ₂ O	FeO	MnO	CaO	Total
	41.791	0	0.002	47.705	0.057	0.044	12.499	0.144	0.213	102.455
	41.791	0.026	0.033	49.221	0.022	0	9.776	0.136	0.046	101.051
	41.409	0	0.042	46.820	0.064	0	12.626	0.238	0.421	101.620
	41.922	0.097	0	47.186	0.010	0.023	11.893	0.243	0.231	101.605
	41.618	0.045	0	48.096	0.060	0.013	11.328	0.124	0.206	101.490
	41.585	0	0	48.254	0.034	0.018	11.623	0.166	0.165	101.845
	40.952	0	0	46.099	0.064	0.010	13.413	0.153	0.204	100.895
	41.840	0.062	0	47.10	0.057	0.032	12.665	0.171	0.150	102.077
	42.371	0.006	0.062	48.525	0.018	0.040	10.915	0.102	0.194	102.233
	41.901	0.083	0.001	48.189	0.051	0.008	10.670	0.133	0.222	101.258
	41.450	0.012	0	47.760	0.042	0.029	10.897	0.152	0.231	100.573
	41.441	0.060	0.018	47.969	0.078	0.003	11.296	0.114	0.164	101.143
	41.607	0.063	0	49.067	0.032	0.032	8.795	0.132	0.160	99.888
	41.470	0.071	0.003	47.916	0.110	0.009	11.878	0.028	0.252	101.737

CH4 – Melilitite (continued)

Oxide	SiO ₂	TiO ₂	K ₂ O	MgO	Al ₂ O ₃	Na ₂ O	FeO	MnO	CaO	Total
	40.908	0	0.046	46.939	0.025	0	12.762	0.166	0.174	101.020
	41.638	0	0.023	47.639	0.059	0.039	11.987	0.072	0.187	101.644
	41.728	0	0.013	48.281	0.038	0.004	11.367	0.107	0.202	101.740
	41.550	0.099	0.007	48.353	0.041	0.029	11.56	0.161	0.262	102.062
	41.588	0	0	49.181	0.005	0	9.771	0.130	0.058	100.733
	41.591	0.079	0.024	49.203	0.016	0.018	9.870	0.090	0.062	100.953
	41.888	0.048	0.019	48.176	0.060	0.023	11.682	0.061	0.221	102.178
	41.397	0	0.034	47.681	0.073	0.036	11.583	0.114	0.221	101.139
	41.929	0	0.011	49.551	0.013	0.019	9.887	0.131	0.063	101.604
	41.657	0	0	47.730	0.043	0.027	12.921	0.187	0.254	102.819
	41.482	0.004	0	47.598	0.013	0.003	12.452	0.102	0.220	101.874
	41.869	0.039	0	47.474	0.037	0.065	11.858	0.184	0.257	101.783
	42.299	0.046	0.024	49.131	0.086	0	10.918	0.138	0.172	102.814
	41.740	0.095	0.009	47.662	0.118	0.046	12.354	0.039	0.188	102.251
	42.218	0	0.004	48.304	0.069	0.011	11.310	0.213	0.161	102.290
	42.307	0.023	0	49.536	0.047	0.001	10.291	0.082	0.146	102.433
	41.282	0.062	0.019	46.641	0.076	0.008	13.073	0.213	0.223	101.597
	41.325	0.039	0	47.509	0.023	0.019	12.546	0.222	0.206	101.889
	42.021	0.001	0	49.776	0.052	0.026	10.322	0.166	0.105	102.469
	41.566	0	0.011	47.563	0.029	0.015	11.755	0.146	0.215	101.300
	42.631	0.005	0	49.988	0.028	0.009	10.066	0.090	0.059	102.876
	41.921	0.042	0.033	46.583	0.038	0.043	13.653	0.208	0.169	102.609
	41.770	0.059	0	47.091	0.042	0.015	12.446	0.114	0.199	101.736
	41.753	0.038	0.022	47.956	0.040	0	11.873	0.113	0.208	102.003
	41.875	0	0	47.872	0.017	0	12.301	0.255	0.225	102.545

CH9 – Melilitite

Oxide	SiO ₂	TiO ₂	K ₂ O	MgO	Al ₂ O ₃	Na ₂ O	FeO	MnO	CaO	Total
CH9	41.335	0.036	0	47.375	0.034	0.003	13.216	0.181	0.198	102.378
	41.815	0	0.001	47.691	0.028	0.041	12.312	0.155	0.167	102.210
	41.907	0	0.017	47.668	0.021	0.039	12.700	0.254	0.173	102.779
	41.879	0.033	0.01	46.934	0.053	0	12.481	0.188	0.183	101.761
	41.709	0.001	0	47.456	0.053	0.020	12.075	0.263	0.171	101.748
	41.713	0.007	0	47.855	0.062	0	12.799	0.180	0.182	102.798
	41.689	0.062	0.007	47.224	0.041	0.018	13.046	0.191	0.190	102.468
	41.493	0.030	0	47.582	0.055	0.033	12.687	0.207	0.170	102.257
	41.717	0.086	0.014	48.077	0.035	0.003	12.320	0.136	0.165	102.553
	41.751	0.017	0	47.884	0.038	0	12.590	0.150	0.137	102.567
	41.504	0.045	0	47.507	0.029	0.054	12.238	0.155	0.158	101.690
	41.778	0	0.003	47.632	0.066	0.009	12.378	0.120	0.134	102.120
	41.583	0.028	0	47.254	0.032	0.011	12.186	0.173	0.178	101.445
	41.575	0.086	0.034	47.44	0.041	0.001	12.572	0.196	0.176	102.121
	41.740	0	0.017	47.693	0.047	0	12.287	0.183	0.171	102.138
	41.248	0	0.025	47.436	0.050	0.025	12.927	0.190	0.149	102.050
	41.656	0	0	47.758	0.036	0.001	12.828	0.214	0.166	102.659
	41.356	0.018	0.010	47.087	0.029	0.038	12.364	0.179	0.190	101.271

CH9 – Melilitite (continued)

Oxide	SiO ₂	TiO ₂	K ₂ O	MgO	Al ₂ O ₃	Na ₂ O	FeO	MnO	CaO	Total
	41.527	0.049	0.028	47.665	0.044	0.018	12.414	0.190	0.184	102.119
	41.615	0.031	0	47.792	0.017	0.040	12.841	0.172	0.199	102.707
	41.450	0.004	0	47.227	0.054	0	12.559	0.113	0.164	101.571
	41.652	0	0	47.838	0.048	0	12.444	0.084	0.165	102.231
	41.797	0	0	46.591	0.080	0.028	13.488	0.150	0.172	102.306
	41.330	0	0.006	47.110	0.052	0.012	13.396	0.117	0.167	102.19
	41.763	0	0	47.359	0.029	0.007	12.474	0.168	0.181	101.981
	41.542	0.077	0	47.707	0.058	0.034	12.426	0.098	0.175	102.117
	41.448	0.074	0.016	47.843	0.049	0.045	12.898	0.130	0.150	102.653
	41.474	0.050	0	47.310	0.037	0.027	12.160	0.181	0.189	101.428
	41.842	0.054	0.041	47.157	0.020	0.008	13.560	0.150	0.170	103.002
	41.588	0.023	0	47.650	0.028	0.017	12.487	0.071	0.176	102.040
	41.602	0.047	0	47.429	0.018	0.020	12.274	0.126	0.21	101.726
	40.750	0.035	0	47.690	0.032	0.013	12.861	0.231	0.146	101.758
	41.483	0.057	0	47.542	0.050	0.008	12.462	0.124	0.163	101.889
	41.733	0	0.031	47.371	0.043	0.024	12.473	0.108	0.150	101.933
	42.070	0.040	0.024	46.950	0.039	0.004	13.816	0.142	0.182	103.267

CH14 – Nephelinite

Oxide	SiO ₂	TiO ₂	K ₂ O	MgO	Al ₂ O ₃	Na ₂ O	FeO	MnO	CaO	Total
	40.543	0	0	45.382	0.069	0.007	14.796	0.152	0.182	101.131
	40.561	0.019	0.001	45.961	0.037	0	13.758	0.136	0.209	100.682
	40.954	0.004	0	45.958	0.049	0.014	13.578	0.155	0.217	100.929
	40.027	0.010	0	43.833	0.026	0.021	15.454	0.171	0.211	99.753
	40.089	0.050	0	43.753	0.060	0.014	15.10	0.170	0.211	99.447
	40.869	0	0.011	46.207	0.046	0.024	12.138	0.165	0.183	99.643
	40.286	0.064	0	46.881	0.020	0.004	12.382	0.105	0.185	99.972
	40.622	0	0.023	47.241	0.038	0	11.588	0.095	0.175	99.782
	40.745	0.002	0.008	47.581	0.039	0.022	11.710	0.226	0.178	100.511
	40.780	0.093	0.01	46.730	0.060	0	11.491	0.128	0.226	99.518
	41.266	0.155	0	47.286	0.032	0.032	11.740	0.108	0.197	100.816
	40.833	0.034	0.022	46.877	0.011	0.003	11.775	0.149	0.208	99.912
	40.745	0	0.031	46.409	0.045	0.005	12.715	0.185	0.259	100.394
	40.853	0.107	0	46.536	0.031	0	12.232	0.177	0.227	100.163
	40.761	0.012	0.007	45.785	0.045	0.051	13.947	0.155	0.214	100.977
	40.989	0	0	47.403	0.006	0	12.425	0.231	0.254	101.308
	41.111	0.087	0	46.983	0.015	0.012	11.970	0.147	0.181	100.506
	41.709	0.132	0.042	47.218	0.057	0.013	12.213	0.195	0.201	101.780
	41.533	0.071	0	46.203	0.093	0.028	13.459	0.244	0.184	101.815
	39.587	0.057	0	46.494	0.079	0.014	12.839	0.159	0.191	99.420
	41.804	0.072	0	47.359	0.050	0	12.592	0.172	0.193	102.242
	41.748	0.056	0.027	47.677	0.044	0.018	12.192	0.208	0.225	102.195
	40.979	0.016	0.009	46.188	0.082	0.016	12.687	0.171	0.197	100.345
	40.015	0.106	0	41.973	0.001	0.056	18.920	0.413	0.336	101.820
	41.487	0	0.010	46.955	0.049	0.021	12.553	0.197	0.181	101.453
	40.979	0.016	0.009	46.188	0.082	0.016	12.687	0.171	0.197	100.345

CH14 – Nephelinite (continued)

Oxide	SiO ₂	TiO ₂	K ₂ O	MgO	Al ₂ O ₃	Na ₂ O	FeO	MnO	CaO	Total
	40.015	0.106	0	41.973	0.001	0.056	18.920	0.413	0.336	101.820
	41.487	0	0.010	46.955	0.049	0.021	12.553	0.197	0.181	101.453
	40.536	0.054	0.002	46.603	0.053	0.004	12.513	0.129	0.217	100.111
	41.188	0	0.002	46.673	0.049	0.006	12.836	0.141	0.201	101.096
	41.177	0.108	0	46.719	0.028	0.035	12.234	0.185	0.212	100.698
	40.122	0	0	44.511	0.055	0.028	14.919	0.150	0.227	100.012
	41.373	0	0.018	47.206	0.051	0.057	11.816	0.196	0.240	100.957
	39.769	0.030	0.010	41.635	0.058	0.030	19.022	0.266	0.203	101.023
	40.990	0.035	0.006	45.762	0.083	0.010	13.288	0.184	0.166	100.524
	41.222	0	0.010	46.324	0.046	0.033	12.092	0.182	0.232	100.141
	40.680	0.018	0.010	43.951	0.044	0.004	16.045	0.146	0.194	101.092
	41.153	0.043	0.007	47.381	0.012	0.018	12.204	0.136	0.173	101.127
	41.190	0.076	0.047	45.875	0.056	0.008	13.524	0.106	0.215	101.097
	40.201	0.077	0.023	45.169	0.021	0.033	14.210	0.128	0.228	100.090

10.2 Mg# calculations

Section	Wt%		Molar weight		wt%/mol w		Mg/(Mg+Fe)
	MgO	FeO	MgO	FeO	Mg	Fe	Mg#
CH 14	44.874	14.631	40.3044	71.8444	1.113	0.204	84.5
	45.650	13.665	40.3044	71.8444	1.133	0.190	85.6
	45.535	13.453	40.3044	71.8444	1.130	0.187	85.8
	46.373	12.181	40.3044	71.8444	1.151	0.170	87.2
	46.894	12.385	40.3044	71.8444	1.163	0.172	87.1
	47.344	11.613	40.3044	71.8444	1.175	0.162	87.9
	47.339	11.650	40.3044	71.8444	1.175	0.162	87.9
	46.956	11.547	40.3044	71.8444	1.165	0.161	87.9
	46.903	11.645	40.3044	71.8444	1.164	0.162	87.8
	46.918	11.785	40.3044	71.8444	1.164	0.164	87.6
	46.460	12.212	40.3044	71.8444	1.153	0.170	87.1
	46.392	11.999	40.3044	71.8444	1.151	0.167	87.3
	45.379	13.219	40.3044	71.8444	1.126	0.184	86.0
	46.765	12.914	40.3044	71.8444	1.160	0.180	86.6
	46.320	12.316	40.3044	71.8444	1.149	0.171	87.0
	46.653	11.930	40.3044	71.8444	1.158	0.166	87.5
	46.029	12.643	40.3044	71.8444	1.142	0.176	86.6
	41.223	18.582	40.3044	71.8444	1.023	0.259	79.8
	46.283	12.373	40.3044	71.8444	1.148	0.172	87.0
	46.551	12.499	40.3044	71.8444	1.155	0.174	86.9
	46.167	12.697	40.3044	71.8444	1.145	0.177	86.6
	46.395	12.149	40.3044	71.8444	1.151	0.169	87.2
	44.506	14.917	40.3044	71.8444	1.104	0.208	84.2
	46.759	11.704	40.3044	71.8444	1.160	0.163	87.7
	41.213	18.829	40.3044	71.8444	1.023	0.262	79.6
	45.523	13.219	40.3044	71.8444	1.129	0.184	86.0
	46.259	12.075	40.3044	71.8444	1.148	0.168	87.2
	43.476	15.872	40.3044	71.8444	1.079	0.221	83.0
	46.853	12.068	40.3044	71.8444	1.162	0.168	87.4
	45.377	13.377	40.3044	71.8444	1.126	0.186	85.8
45.128	14.197	40.3044	71.8444	1.120	0.198	85.0	
CH9	46.275	12.909	40.3044	71.8444	1.148	0.180	86.5
	46.660	12.046	40.3044	71.8444	1.158	0.168	87.3
	46.379	12.357	40.3044	71.8444	1.151	0.172	87.0
	46.122	12.265	40.3044	71.8444	1.144	0.171	87.0
	46.641	11.868	40.3044	71.8444	1.157	0.165	87.5
	46.552	12.451	40.3044	71.8444	1.155	0.173	87.0
	46.087	12.732	40.3044	71.8444	1.143	0.177	86.6
	46.532	12.407	40.3044	71.8444	1.155	0.173	87.0
	46.880	12.013	40.3044	71.8444	1.163	0.167	87.4
	46.686	12.275	40.3044	71.8444	1.158	0.171	87.1
	46.717	12.035	40.3044	71.8444	1.159	0.168	87.4

Section	Wt%		Molar weight		wt%/mol w		Mg/(Mg+Fe)
	MgO	FeO	MgO	FeO	Mg	Fe	Mg#
CH9	46.643	12.121	40.3044	71.8444	1.157	0.169	87.3
	46.581	12.012	40.3044	71.8444	1.156	0.167	87.4
	46.455	12.311	40.3044	71.8444	1.153	0.171	87.1
	46.695	12.030	40.3044	71.8444	1.159	0.167	87.4
	46.483	12.667	40.3044	71.8444	1.153	0.176	86.7
	46.521	12.496	40.3044	71.8444	1.154	0.174	86.9
	46.496	12.209	40.3044	71.8444	1.154	0.170	87.2
	46.676	12.156	40.3044	71.8444	1.158	0.169	87.3
	46.532	12.503	40.3044	71.8444	1.155	0.174	86.9
	46.497	12.365	40.3044	71.8444	1.154	0.172	87.0
	46.794	12.172	40.3044	71.8444	1.161	0.169	87.3
	45.541	13.184	40.3044	71.8444	1.130	0.184	86.0
	46.100	13.109	40.3044	71.8444	1.144	0.182	86.2
	46.439	12.232	40.3044	71.8444	1.152	0.170	87.1
	46.718	12.168	40.3044	71.8444	1.159	0.169	87.3
	46.607	12.565	40.3044	71.8444	1.156	0.175	86.9
	46.644	11.989	40.3044	71.8444	1.157	0.167	87.4
	45.783	13.165	40.3044	71.8444	1.136	0.183	86.1
	46.697	12.237	40.3044	71.8444	1.159	0.170	87.2
	46.624	12.066	40.3044	71.8444	1.157	0.168	87.3
46.866	12.639	40.3044	71.8444	1.163	0.176	86.9	
46.661	12.231	40.3044	71.8444	1.158	0.170	87.2	
46.473	12.236	40.3044	71.8444	1.153	0.170	87.1	
45.465	13.379	40.3044	71.8444	1.128	0.186	85.8	
CH23	44.668	14.205	40.3044	71.8444	1.108	0.198	84.9
	44.949	13.888	40.3044	71.8444	1.115	0.193	85.2
	45.362	13.872	40.3044	71.8444	1.125	0.193	85.4
	45.981	12.629	40.3044	71.8444	1.141	0.176	86.6
	45.996	12.805	40.3044	71.8444	1.141	0.178	86.5
	44.980	14.021	40.3044	71.8444	1.116	0.195	85.1
	41.887	17.550	40.3044	71.8444	1.039	0.244	81.0
	45.175	13.939	40.3044	71.8444	1.121	0.194	85.2
	46.431	11.888	40.3044	71.8444	1.152	0.165	87.4
	44.036	15.240	40.3044	71.8444	1.093	0.212	83.7
	46.528	11.963	40.3044	71.8444	1.154	0.167	87.4
	44.985	14.238	40.3044	71.8444	1.116	0.198	84.9
	41.941	19.100	40.3044	71.8444	1.041	0.266	79.7
	45.134	13.995	40.3044	71.8444	1.120	0.195	85.2
	46.168	12.512	40.3044	71.8444	1.145	0.174	86.8
	42.472	16.716	40.3044	71.8444	1.054	0.233	81.9
	46.319	12.430	40.3044	71.8444	1.149	0.173	86.9
	45.695	13.053	40.3044	71.8444	1.134	0.182	86.2
	44.698	14.130	40.3044	71.8444	1.109	0.197	84.9
	45.020	14.106	40.3044	71.8444	1.117	0.196	85.1

Section	Wt%		Molar weight		wt%/mol w		Mg/(Mg+Fe)
	MgO	FeO	MgO	FeO	Mg	Fe	Mg#
CH23	45.270	13.619	40.3044	71.8444	1.123	0.190	85.6
	46.266	12.286	40.3044	71.8444	1.148	0.171	87.0
	44.992	13.915	40.3044	71.8444	1.116	0.194	85.2
CH4	46.562	12.200	40.3044	71.8444	1.155	0.170	87.2
	47.390	11.162	40.3044	71.8444	1.176	0.155	88.3
	47.380	11.412	40.3044	71.8444	1.176	0.159	88.1
	45.690	13.294	40.3044	71.8444	1.134	0.185	86.0
	46.142	12.407	40.3044	71.8444	1.145	0.173	86.9
	47.465	10.677	40.3044	71.8444	1.178	0.149	88.8
	47.590	10.537	40.3044	71.8444	1.181	0.147	89.0
	47.488	10.835	40.3044	71.8444	1.178	0.151	88.7
	47.427	11.168	40.3044	71.8444	1.177	0.155	88.3
	49.122	8.805	40.3044	71.8444	1.219	0.123	90.9
	47.098	11.675	40.3044	71.8444	1.169	0.163	87.8
	46.465	12.633	40.3044	71.8444	1.153	0.176	86.8
	46.868	11.793	40.3044	71.8444	1.163	0.164	87.6
	47.455	11.173	40.3044	71.8444	1.177	0.156	88.3
	47.376	11.326	40.3044	71.8444	1.175	0.158	88.2
	48.823	9.700	40.3044	71.8444	1.211	0.135	90.0
	48.739	9.777	40.3044	71.8444	1.209	0.136	89.9
	47.149	11.433	40.3044	71.8444	1.170	0.159	88.0
	47.144	11.453	40.3044	71.8444	1.170	0.159	88.0
	47.786	10.619	40.3044	71.8444	1.186	0.148	88.9
	46.613	12.082	40.3044	71.8444	1.157	0.168	87.3
	47.223	11.057	40.3044	71.8444	1.172	0.154	88.4
	48.359	10.047	40.3044	71.8444	1.200	0.140	89.6
	45.908	12.868	40.3044	71.8444	1.139	0.179	86.4
46.628	12.313	40.3044	71.8444	1.157	0.171	87.1	
47.014	11.640	40.3044	71.8444	1.166	0.162	87.8	
46.684	11.996	40.3044	71.8444	1.158	0.167	87.4	
Core	48.709	9.674	40.3044	71.8444	1.209	0.135	90.0
Rim	46.074	12.425	40.3044	71.8444	1.143	0.173	86.9
Pheno	46.441	11.705	40.3044	71.8444	1.152	0.163	87.6
Core	48.769	9.731	40.3044	71.8444	1.210	0.135	89.9
Rim	46.421	12.567	40.3044	71.8444	1.152	0.175	86.8
Rim	46.722	12.223	40.3044	71.8444	1.159	0.170	87.2
Pheno	46.642	11.650	40.3044	71.8444	1.157	0.162	87.7
Core	48.577	10.073	40.3044	71.8444	1.205	0.140	89.6
Rim	46.953	11.604	40.3044	71.8444	1.165	0.162	87.8
Core	48.591	9.785	40.3044	71.8444	1.206	0.136	89.8
Rim	45.363	13.295	40.3044	71.8444	1.126	0.185	85.9
pheno	46.287	12.234	40.3044	71.8444	1.148	0.170	87.1

10.3 K_D calculations

10.3.1 K_D Calculations

Sample #	FeO/MgO Pheno		Melt X		Kd Calc	KD	FeO _{oi} / (K _D *MgO _{oi})
	MgO	FeO	MgO	FeO*			
CH14	44.87	14.63	12.12	11.31	0.35	0.30	1.09
	45.65	13.66	12.12	11.31	0.32	0.30	1.00
	45.53	13.45	12.12	11.31	0.32	0.30	0.98
	46.37	12.18	12.12	11.31	0.28	0.30	0.88
	46.89	12.39	12.12	11.31	0.28	0.30	0.88
	47.34	11.61	12.12	11.31	0.26	0.30	0.82
	47.34	11.65	12.12	11.31	0.26	0.30	0.82
	46.96	11.55	12.12	11.31	0.26	0.30	0.82
	46.90	11.64	12.12	11.31	0.27	0.30	0.83
	46.92	11.79	12.12	11.31	0.27	0.30	0.84
	46.46	12.21	12.12	11.31	0.28	0.30	0.88
	46.39	12.00	12.12	11.31	0.28	0.30	0.86
	45.38	13.22	12.12	11.31	0.31	0.30	0.97
	46.77	12.91	12.12	11.31	0.30	0.30	0.92
	46.32	12.32	12.12	11.31	0.28	0.30	0.89
	46.65	11.93	12.12	11.31	0.27	0.30	0.85
	46.03	12.64	12.12	11.31	0.29	0.30	0.92
	41.22	18.58	12.12	11.31	0.48	0.30	1.50
	46.28	12.37	12.12	11.31	0.29	0.30	0.89
	46.55	12.50	12.12	11.31	0.29	0.30	0.90
	46.17	12.70	12.12	11.31	0.29	0.30	0.92
	46.40	12.15	12.12	11.31	0.28	0.30	0.87
	44.51	14.92	12.12	11.31	0.36	0.30	1.12
	46.76	11.70	12.12	11.31	0.27	0.30	0.83
	41.21	18.83	12.12	11.31	0.49	0.30	1.52
	45.52	13.22	12.12	11.31	0.31	0.30	0.97
	46.26	12.07	12.12	11.31	0.28	0.30	0.87
	43.48	15.87	12.12	11.31	0.39	0.30	1.22
	46.85	12.07	12.12	11.31	0.28	0.30	0.86
	45.38	13.38	12.12	11.31	0.32	0.30	0.98
45.13	14.20	12.12	11.31	0.34	0.30	1.05	
CH9	46.27	12.91	13.37	11.80	0.32	0.30	0.93
	46.66	12.05	13.37	11.80	0.29	0.30	0.86
	46.38	12.36	13.37	11.80	0.30	0.30	0.89
	46.12	12.27	13.37	11.80	0.30	0.30	0.89
	46.64	11.87	13.37	11.80	0.29	0.30	0.85
	46.55	12.45	13.37	11.80	0.30	0.30	0.89
	46.09	12.73	13.37	11.80	0.31	0.30	0.92
	46.53	12.41	13.37	11.80	0.30	0.30	0.89
	46.88	12.01	13.37	11.80	0.29	0.30	0.85
	46.69	12.27	13.37	11.80	0.30	0.30	0.88
	46.72	12.03	13.37	11.80	0.29	0.30	0.86
	46.64	12.12	13.37	11.80	0.29	0.30	0.87

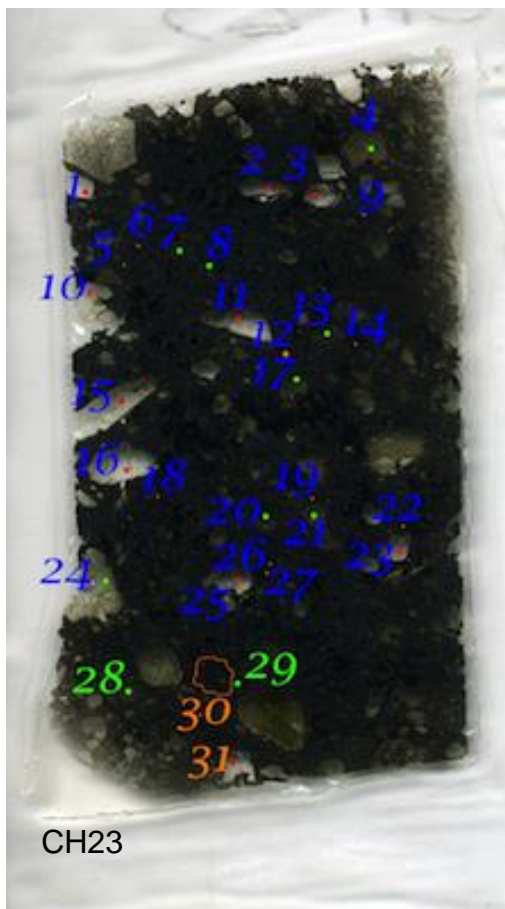
Sample #	FeO/MgO Pheno		Melt X		Kd Calc	KD	FeO _{Ol} / (K _D *MgO _{Ol})
	MgO	FeO	MgO	FeO*			
CH9	46.58	12.01	13.37	11.80	0.29	0.30	0.86
	46.45	12.31	13.37	11.80	0.30	0.30	0.88
	46.69	12.03	13.37	11.80	0.29	0.30	0.86
	46.48	12.67	13.37	11.80	0.31	0.30	0.91
	46.52	12.50	13.37	11.80	0.30	0.30	0.90
	46.50	12.21	13.37	11.80	0.30	0.30	0.88
	46.68	12.16	13.37	11.80	0.30	0.30	0.87
	46.53	12.50	13.37	11.80	0.30	0.30	0.90
	46.50	12.36	13.37	11.80	0.30	0.30	0.89
	46.79	12.17	13.37	11.80	0.29	0.30	0.87
	45.54	13.18	13.37	11.80	0.33	0.30	0.96
	46.10	13.11	13.37	11.80	0.32	0.30	0.95
	46.44	12.23	13.37	11.80	0.30	0.30	0.88
	46.72	12.17	13.37	11.80	0.30	0.30	0.87
	46.61	12.56	13.37	11.80	0.31	0.30	0.90
	46.64	11.99	13.37	11.80	0.29	0.30	0.86
	45.78	13.16	13.37	11.80	0.33	0.30	0.96
	46.70	12.24	13.37	11.80	0.30	0.30	0.87
	46.62	12.07	13.37	11.80	0.29	0.30	0.86
	46.87	12.64	13.37	11.80	0.31	0.30	0.90
46.66	12.23	13.37	11.80	0.30	0.30	0.87	
46.47	12.24	13.37	11.80	0.30	0.30	0.88	
45.46	13.38	13.37	11.80	0.33	0.30	0.98	
CH23	44.67	14.20	11.60	11.00	0.34	0.30	1.06
	44.95	13.89	11.60	11.00	0.33	0.30	1.03
	45.36	13.87	11.60	11.00	0.32	0.30	1.02
	45.98	12.63	11.60	11.00	0.29	0.30	0.92
	46.00	12.80	11.60	11.00	0.29	0.30	0.93
	44.98	14.02	11.60	11.00	0.33	0.30	1.04
	41.89	17.55	11.60	11.00	0.44	0.30	1.40
	45.18	13.94	11.60	11.00	0.33	0.30	1.03
	46.43	11.89	11.60	11.00	0.27	0.30	0.85
	44.04	15.24	11.60	11.00	0.37	0.30	1.15
	46.53	11.96	11.60	11.00	0.27	0.30	0.86
	44.98	14.24	11.60	11.00	0.33	0.30	1.06
	41.94	19.10	11.60	11.00	0.48	0.30	1.52
	45.13	13.99	11.60	11.00	0.33	0.30	1.03
	46.17	12.51	11.60	11.00	0.29	0.30	0.90
	42.47	16.72	11.60	11.00	0.42	0.30	1.31
	46.32	12.43	11.60	11.00	0.28	0.30	0.89
	45.70	13.05	11.60	11.00	0.30	0.30	0.95
	44.70	14.13	11.60	11.00	0.33	0.30	1.05
	45.02	14.11	11.60	11.00	0.33	0.30	1.04
45.27	13.62	11.60	11.00	0.32	0.30	1.00	
46.27	12.29	11.60	11.00	0.28	0.30	0.89	
44.99	13.91	11.60	11.00	0.33	0.30	1.03	
CH4	46.56	12.20	13.37	11.80	0.30	0.30	0.87

Sample #	FeO/MgO Pheno		Melt X		Kd Calc	KD	FeO _{Ol} / (K _D *MgO _{Ol})
	MgO	FeO	MgO	FeO*			
CH4	47.39	11.16	13.37	11.80	0.27	0.30	0.79
	47.38	11.41	13.37	11.80	0.27	0.30	0.80
	45.69	13.29	13.37	11.80	0.33	0.30	0.97
	46.14	12.41	13.37	11.80	0.30	0.30	0.90
	47.47	10.68	13.37	11.80	0.25	0.30	0.75
	47.59	10.54	13.37	11.80	0.25	0.30	0.74
	47.49	10.83	13.37	11.80	0.26	0.30	0.76
	47.43	11.17	13.37	11.80	0.27	0.30	0.78
	49.12	8.80	13.37	11.80	0.20	0.30	0.60
	47.10	11.68	13.37	11.80	0.28	0.30	0.83
	46.47	12.63	13.37	11.80	0.31	0.30	0.91
	46.87	11.79	13.37	11.80	0.29	0.30	0.84
	47.46	11.17	13.37	11.80	0.27	0.30	0.78
	47.38	11.33	13.37	11.80	0.27	0.30	0.80
	48.82	9.70	13.37	11.80	0.23	0.30	0.66
	48.74	9.78	13.37	11.80	0.23	0.30	0.67
	47.15	11.43	13.37	11.80	0.27	0.30	0.81
	47.14	11.45	13.37	11.80	0.28	0.30	0.81
	47.79	10.62	13.37	11.80	0.25	0.30	0.74
	46.61	12.08	13.37	11.80	0.29	0.30	0.86
	47.22	11.06	13.37	11.80	0.27	0.30	0.78
	48.36	10.05	13.37	11.80	0.24	0.30	0.69
	45.91	12.87	13.37	11.80	0.32	0.30	0.93
	46.63	12.31	13.37	11.80	0.30	0.30	0.88
	47.01	11.64	13.37	11.80	0.28	0.30	0.83
	46.68	12.00	13.37	11.80	0.29	0.30	0.86
Core	48.71	9.67	13.37	11.80	0.23	0.30	0.66
Rim	46.07	12.42	13.37	11.80	0.31	0.30	0.90
Pheno	46.44	11.71	13.37	11.80	0.29	0.30	0.84
Core	48.77	9.73	13.37	11.80	0.23	0.30	0.67
Rim	46.42	12.57	13.37	11.80	0.31	0.30	0.90
Rim	46.72	12.22	13.37	11.80	0.30	0.30	0.87
Pheno	46.64	11.65	13.37	11.80	0.28	0.30	0.83
Core	48.58	10.07	13.37	11.80	0.23	0.30	0.69
Rim	46.95	11.60	13.37	11.80	0.28	0.30	0.82
Core	48.59	9.78	13.37	11.80	0.23	0.30	0.67
Rim	45.36	13.30	13.37	11.80	0.33	0.30	0.98
Pheno	46.29	12.23	13.37	11.80	0.30	0.30	0.88

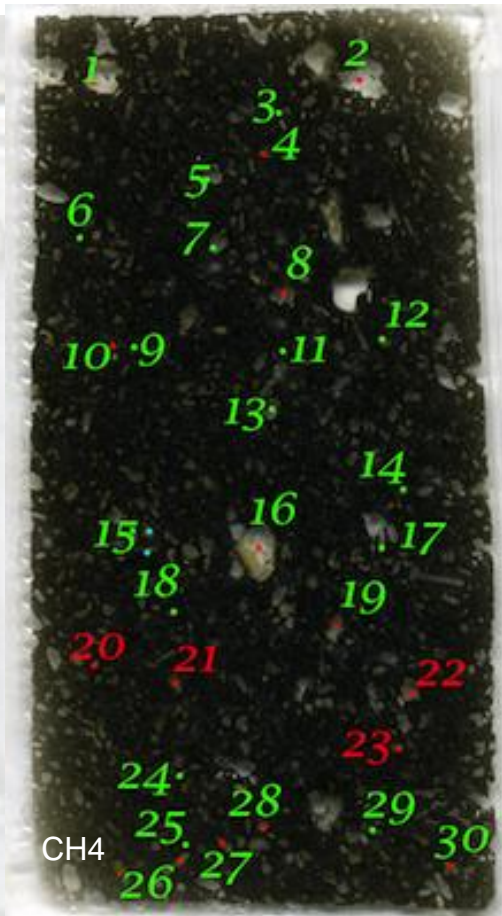
10.3.2 FeO/MgO ratio whole rock composition

Melilitite			Nephelinite			Basalt		
MgO	FeO*	Melt ratio	MgO	FeO*	Melt ratio	MgO	FeO*	Melt ratio
14.15	10.99	0.78	11.58	10.46	0.90	11.10	10.19	0.92
14.15	10.99	0.78	12.10	10.79	0.89	11.10	10.19	0.92
11.78	11.25	0.96	12.20	11.18	0.92	11.20	10.74	0.96
11.83	11.37	0.96	12.20	11.18	0.92	11.20	10.74	0.96
13.83	11.57	0.84	12.22	11.41	0.93	11.77	10.74	0.91
13.83	11.57	0.84	9.03	11.57	1.28	12.36	11.38	0.92
15.50	11.62	0.75	13.81	11.95	0.87	12.36	11.38	0.92
15.50	11.62	0.75	13.81	11.95	0.87	9.57	11.42	1.19
12.12	11.80	0.97				12.68	11.59	0.91
12.90	12.04	0.93				12.68	11.59	0.91
16.70	12.12	0.73						
12.51	12.20	0.98						
9.08	12.21	1.34						
13.02	12.22	0.94						
13.49	12.60	0.93						
13.49	12.60	0.93						
Average melt X			Average melt X			Average melt X		
12.119	11.311		13.3675	11.798		11.602	10.996	

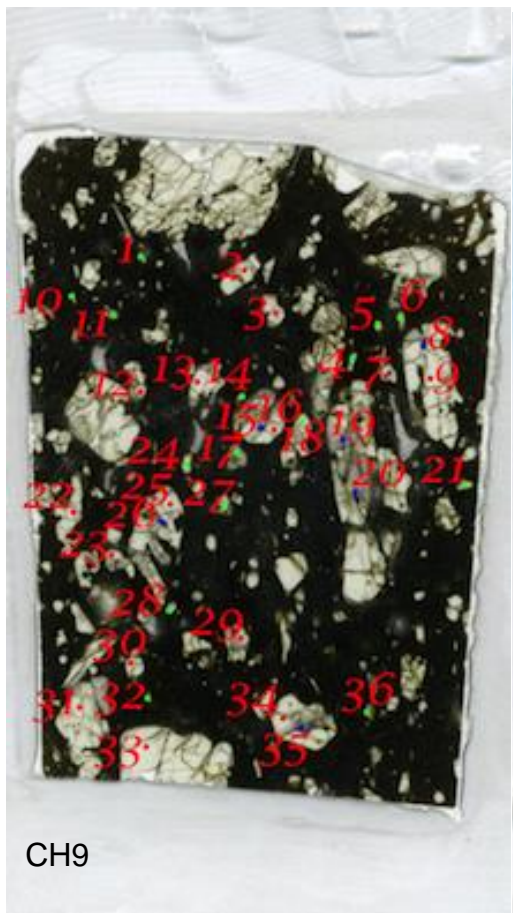
10.5 Thin section photographs with marked analytical points



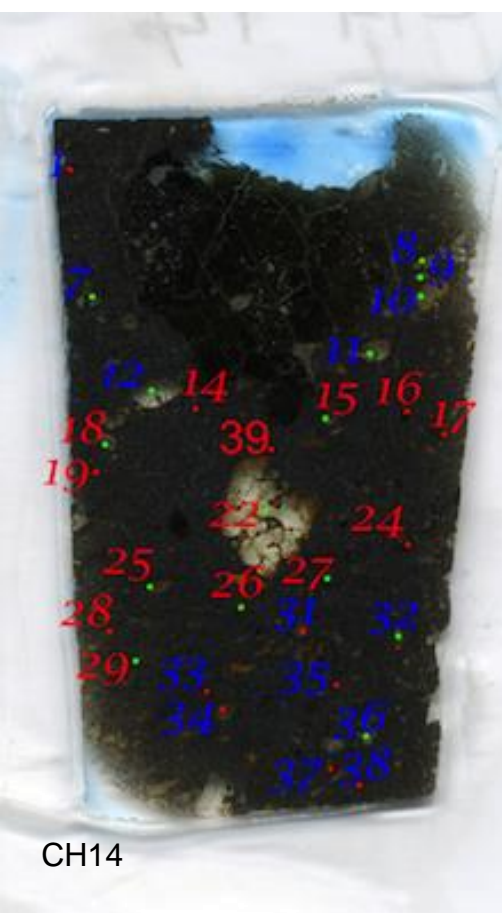
CH23



CH4



CH9



CH14